1 **High-precision atmospheric oxygen measurement comparisons between a newly built**

2 **CRDS analyzer and existing measurement techniques**

4 Tesfaye A. Berhanu[1,2], John Hoffnagle[2], Chris Rella[2], David Kimhak[2], Peter Nyfeler[1], Markus

5 Leuenberger[1]

6 [1]*Climate and Environmental Physics, Physics Institute and Oeschger Centre for Climate Change Research,*

7 *University of Bern, Bern, Switzerland*

8 [2]*Picarro Inc., 3105 Patrick Henry Drive, Santa Clara, CA, USA*

10 **Abstract**

11 Carbon dioxide and oxygen are tightly coupled in land-biospheres CO_2 - O_2 exchange

12 processes, while they are not coupled in oceanic exchange. For this reason, atmospheric

13 oxygen measurements can be used to constrain the global carbon cycle, especially oceanic

14 uptake. However, accurately quantifying the small (~1-100 ppm) variations in O_2 is

15 analytically challenging due to the very large atmospheric background which constitutes

16 about 20.9 % (~209500 ppm) of atmospheric air. Here we present a detailed description of the

17 analyzer and its operating principles as well as comprehensive laboratory and field studies for

18 a newly developed high-precision oxygen mixing ratio and isotopic composition analyzer

19 (Picarro G-2207) that is based on cavity ring-down spectroscopy (CRDS). From the

20 laboratory tests, we have calculated a short-term precision (standard error of one-minute O_2

21 mixing ratio measurements) of < 1 ppm for this analyzer based on measurements of eight

22 standard gases analyzed for two hours consecutively. In contrast to the currently existing

23 techniques, the instrument has an excellent long-term stability and therefore a calibration

24 every 12 hours is sufficient to get an overall uncertainty of < 5 ppm. Measurements of

ambient air were also conducted at the High-Altitude Research Station, Jungfraujoch and the Beromünster tall tower in Switzerland. At both sites, we observed opposing and diurnally varying CO_2 and O_2 profiles due to different processes such as combustion, photosynthesis and respiration. Based on the combined measurements at Beromünster tower, we determined height dependent O_2:CO_2 oxidation ratios varying between -0.98 to -1.60 , which increase with the height of the tower inlet, possibly due to different source contribution such as natural gas combustion with high oxidation ratio and biological processes which are at the lower end.

1. Introduction

Atmospheric oxygen comprises about 20.9 % of the global atmosphere and in the past decade its concentration decreased at a rate of $\sim$ 20 per meg yr-1 (Keeling and Manning, 2014) mainly associated with the increase in fossil fuel combustion. Measurements of atmospheric O_2 are reported as the ratio to the N_2 concentration and expressed as $\delta(O_2/N_2)$ because the variations in the concentrations of other atmospheric gases such as CO_2 can influence the O_2 partial pressure while this ratio is insensitive to these changes in other gases. These variations in atmospheric O_2 is commonly expressed in units of per meg due to its small variations with respect to a large background, where

$$\delta \left(\frac{O_2}{N_2} \right) (per\ meg) = \left(\frac{(\frac{O_2}{N_2})_{sample}}{(\frac{O_2}{N_2})_{reference}} - 1 \right) . 10^6 \qquad (1)$$

Note that we convert per meg to parts per million equivalent by multiplying per meg by 0.209500 (the O_2 mole fraction of atmospheric air).

In contrast to O_2, the global average atmospheric CO_2 mixing ratio increased to 405.0 ppm averaged over 2017 since its preindustrial value of 280 ppm (Le Quéré et al., 2017). As the variability of atmospheric oxygen is directly linked to the carbon cycle, both its short and long-term observations can be used to better constrain the carbon cycle. For example, since

48 first suggested by Keeling and Shertz (1992) the long-term trends derived from concurrent

49 measurements of atmospheric CO_2 and O_2 have been widely used to quantify the partitioning

50 of atmospheric CO_2 between the land-biosphere and oceanic sinks (Battle et al., 2000; Goto et

51 al., 2017; Manning and Keeling, 2006; Valentino et al., 2008). This method hinges on the

52 linear coupling between CO_2 and O_2 with an oxidation ratio (OR, defined as the

53 stoichiometric ratio of exchange during various process such as photosynthesis and respiration

54 expressed using α) of 1.1 for the terrestrial biosphere photosynthesis-respiration processes

55 ($α_b$) and 1.4 for fossil fuel combustion ($α_f$) while they are decoupled for oceanic processes ($α_o$

56 = 0). Meanwhile, the short-term variability in atmospheric oxygen can be used to estimate

57 marine biological productivity and air-sea gas exchange (Keeling et al., 1998; Nevison et al.,

58 2012). However, the accuracy of these estimates is primarily linked to the accuracy and

59 precision of atmospheric O_2 measurements and the assumed ORs for the different processes

60 which are highly variable in contrast to atmospheric CO_2 that can be well measured within the

61 precision guidelines set by the Global Atmospheric Watch (GAW) (± 0.1 ppm for the

62 northern hemisphere).

63 Currently there are several, mostly custom built techniques that can measure

64 atmospheric O_2 variations as oxygen concentration based on interferometric, paramagnetic,

65 UV absorption and fuel cell technology (Keeling, 1988a; Manning et al., 1999; Stephens et

66 al., 2007) or as O_2/N_2 ratios to account for the large background effect using gas

67 chromatography with thermal conductivity detector (GC-TCD) or gas chromatography

68 coupled to mass spectrometry (GC-MS) (Bender et al., 1994; Tohjima, 2000). Despite the fact

69 that these techniques have been used for more than two decades, accurate quantification of

70 atmospheric oxygen variability remains challenging primarily because the small ppm-level

71 atmospheric oxygen signal rides on a ~ 210,000 ppm background, which places stringent

72 requirements on the precision and drift of the analysis methods especially for continuous

73 monitoring(note that the GAW recommendation for the measurement precision of O_2/N_2 is 2

74 per meg). The techniques listed above struggle to routinely achieve the necessary performance

75 for various reasons, including i) instability over time that requires frequent measurement

76 interruption for calibration, ii) measurement bias with ambient and sample temperature and/or

77 pressure, and/or iii) systematic errors in the measurement due to other atmospheric species.

78 Further, some techniques require the use of consumables and rely on high vacuum, which

79 complicates field deployment.

80 In this manuscript we describe a new high precision oxygen concentration and isotopic

81 composition analyzer by Picarro Inc., Santa Clara, USA (G-2207) based on CRDS

82 technology. Here, we will introduce the analyzer design principles in details, describe the

83 unique features of the analyzer and evaluate its performance based on various independent

84 laboratory and field tests by comparing it with currently existing techniques. Then, we will

85 present and interpret our observations based on field measurements. Finally, we will conclude

86 its overall performance and provide recommendations and possible improvements.

87 **2. Analyzer design principles**

88 The analyzer described here is derived from the Picarro G2000 series of CRDS

89 analyzers. The basic elements have been described elsewhere (Crosson, 2008; Martin et al.,

90 2016; Steig et al., 2014): briefly, the instrument is built around a high-finesse, traveling-wave

91 optical cavity, which is coupled to either of two single-frequency Distributed FeedBack-

92 stabilized semiconductor lasers. One cavity mirror is mounted on a piezoelectric translator

93 (PZT) to allow fine tuning of the cavity resonance frequencies. A semiconductor optical

94 amplifier between the laser sources and the cavity boosts the laser power and serves as a fast-

95 optical switch. The cavity body is constructed of invar and enclosed in a temperature

96 stabilized box (T = 45° C, stabilized to approximately 0.01 °C) for dimensional and

97 spectroscopic stability. A vacuum pump pulls the gas to be sampled through the cavity and a

98 proportional valve between the cavity and the pump maintains the sample pressure in the

99 cavity at a value of 340 hPa, with variations on the order of 1 Pa. The instrument has a

100 wavelength monitor, based upon measurements of interference fringes from a solid etalon,

101 which is used to control the laser wavelength by adjusting the laser temperature and current.

102 The wavelength monitor is a fiber-coupled device located between the laser and the cavity. A

103 fraction of the beam from the input fiber is collected using a beam splitter for the

104 measurement wavelength and the remaining power is collected in the output fiber. A high-

105 speed photodiode monitors the optical power emerging from the cavity. The instrument's data

106 acquisition system is used to sweep the laser frequency over the spectral feature to be

107 measured, modulates the laser output to initiate ring-downs, and fits the ring-down signal to

108 an exponential function to generate a spectrogram of optical loss versus laser frequency. For

109 this instrument the empty cavity ring-down time constant is about 39 μs. Subsequent program

110 modules compare the measured loss spectrum to a spectral model, using non-linear least-

111 squares fitting (Press et al., 1986) to find the best-fit model parameters and thereby obtain a

112 quantitative measure of the absorption due to the target molecule, and finally apply a

113 calibration factor to the optical absorption to deduce the molecular concentration. When

114 operating in its normal gas analysis mode, the instrument acquires about 200-300 ring-downs

115 per second and achieves a noise equivalent absorption of typically about 10^{-11} cm^{-1} Hz$^{-1/2}$,

116 with some variation between instruments.

117   The primary goal when designing this analyzer was to measure the molecular oxygen

118 concentration with few-per-meg level precision and stability. In this context operational

119 stability is as important as signal-to-noise. Our experience has been that the most stable

operation of the analyzer is achieved when the optical phase length of the cavity is held as nearly constant as possible. In this case the free spectral range (FSR, 0.0206 cm^{-1}) of the temperature stabilized, invar ring-down cavity provides a better optical frequency standard than the etalon-based wavelength monitor, which in turn allows more consistent measurements of absorption line width and integrated absorption line intensity (Steig et al., 2014). For a small, field-deployable instrument, it is not practical to stabilize the absolute frequencies of the cavity modes to an optical frequency standard (Hodges et al., 2004) but the oxygen lines themselves, under conditions of constant temperature and pressure, provide an adequate frequency reference. The oxygen spectrum was also used to calibrate the FSR, by comparing a wide (approximately 10 cm^{-1}) FSR-spaced spectrum with the Hitran database (Rothman et al., 2013).

To determine molecular oxygen concentration, the analyzer measures absorption of the Q13Q13 component of the $a^1\Delta_g \leftarrow X^3\Sigma^-_g$ band, at 7878.805547 cm^{-1}, according to the latest edition of Hitran (Gordon et al., 2017). This is one of the strongest near-infrared lines of oxygen, well separated from other oxygen lines, and reasonably free of spectral interference from water, carbon dioxide, methane, and other constituents of clean air. The spectral model for this line was developed using reference spectra of clean, dry, synthetic air that were acquired with the same hardware as in the field-deployable analyzer, but with special-purpose software that allows it to operate as a more general spectrometer.

Recently, considerable work has been done to advance the understanding of spectral line shapes and to define functional representations that better describe the processes that determine spectral line shapes than does the Voigt model (Hartmann et al., 2008; Tennyson et al., 2014, Tran et al., 2019). Line shape studies have been published for the 1.27 µm band of O_2 (Fleisher et al., 2015; Lamouroux et al., 2014), though not to our knowledge for the Q

branch. The apparatus used here is not capable of spectroscopic studies of comparable precision; the absolute temperature and pressure monitoring and especially the frequency metrology are far too crude for that purpose. Our goal is merely to define a simple model of the Q13Q13 line that is adequate for least-squares retrievals of the O_2 absorption under the limited range of conditions (stabilized temperature and pressure) that the operational analyzer experiences in the field. The CRDS analyzers use the Galatry function (Varghese and Hanson, 1984), which is distinctly better than the Voigt and still easily and quickly evaluated for line shape modeling. Ultimately, the usefulness of the spectral model is to be evaluated by the precision and stability of the O_2 measurements when compared with established techniques. Ultimately, the usefulness of the spectral model is to be evaluated by the precision and stability of the O_2 measurements when compared with established techniques.For spectral model development, this spectrometer has the drawback that the cavity FSR, is too large to reveal much detail of the absorption line shape, even with the simplifying assumption of a Galatry line shape. We therefore acquired a set of four interleaved spectra, with the PZT-actuated mirror moved to offset the cavity modes of the individual FSR-spaced spectra by one-fourth of an FSR. The precise offsets were determined from fits to the strong and well-isolated O_2 lines in the spectra. From the consistency of the fitted line centers, we estimate that the positioning of the interleaved spectra was accurate to approximately 10 MHz. The spectrum of the Q13Q13 line acquired in this manner is shown in Figure 1, together with the best-fit Galatry function. It stands out that the residuals are largely odd in detuning from the line center: this shows the limitations of the Galatry model in this case, since the Galatry function is purely even about the line center. The shape of the absorption line in this model is specified by two dimensionless parameters: the collisional broadening parameter

$$y = \gamma / \sigma_D \tag{2}$$

168   and the collisional narrowing parameter

169    $z = \beta / \sigma_D$ (3)

170   where γ is the frequency of broadening transitions, β is the velocity change collision rate, and

171   σ_D is the 1/e Doppler half-width of the transition, given by

172    $\sigma_D = \nu_0 (2k_B T / Mc^2)^{1/2}$ (4)

173   where ν_0 is the transition frequency, k_B is Boltzmann's constant (J. K^{-1}), T is the sample

174   temperature (K), M is the molecular mass (amu), and c is the speed of light (m/s). Figure 2

175   shows the values of y and z obtained from spectra acquired in the same way as Figure 1, as a

176   function of cavity pressure. The values depend linearly on pressure, as expected from the

177   Galatry model, but the unconstrained linear fits do not go precisely through the origin. It is

178   not clear whether this represents a breakdown of the Galatry model or simply reflects the

179   limited quality of the data set. The slope of y can be converted to an air-broadened collisional

180   width γ_{air} = 0.0442 cm^{-1}/atm, which agrees with the Hitran value of 0.0460 cm^{-1}/atm (Gordon

181   et al., 2016) to within the uncertainty estimate stated by Hitran (uncertainty code 4 for γ_{air}

182   corresponding to 10% --20% relative uncertainty). The slope of z can be interpreted in terms of

183   the optical diffusion coefficient (Fleisher et al., 2015), yielding D = 0.285 cm^2 s^{-1}, compared

184   to the literature value of 0.233 cm^2 s^{-1} for O_2 in air at 45 °C (Marrero and Mason, 1972).

185   Although the anticipated use of the analyzer is for ambient air samples having a very small

186   range of O_2 concentrations, we did investigate the variation of the line shape in binary

187   mixtures of O_2 and N_2 shown in Figure 3. The error bars are taken from the output of the

188   Levenberg-Marquardt fitting routine (Press et al., 1992). The dependence of the collisional

189   broadening parameter z on O_2 mole fraction was considered too small to be significant, but

190   the variation in y was used in the subsequent analysis of the air samples. Note that Wójtewicz

191   et al. (Wójtewicz et al., 2014) also found collisional broadening coefficients for nitrogen to be

192   slightly larger than for oxygen in measurements of one O_2 line in the B-band.

193   The primary goal in designing the analyzer was to achieve high enough precision to

194   make meaningful measurements of O_2 in clean atmospheric samples. Although the current

195   best practice for such high-precision measurements is to work with dried samples, we decided

196   to include high precision measurements of water vapor. There were two reasons for this

197   decision: one is to serve as a monitor for residual water vapor, which is difficult to remove

198   completely from the ring-down cavity and associated sample handling hardware, and the

199   second and more ambitious reason was to see how well the effect of water vapor could be

200   corrected for measurements of undried ambient air. While it was considered unlikely that

201   measurements of undried air could compete in accuracy with those of dried air, it might be

202   possible to correct for water vapor well enough to enable useful measurements in some

203   circumstances without the expense and inconvenience of drying the sample. For this purpose,

204   a second laser was added, which probes the $7_{1,6} \rightarrow 8_{4,5}$ component of the $2v_3$ band of water

205   vapor, at of 7816.75210 cm^{-1} (Gordon et al., 2017). The Galatry model was used to fit spectra

206   of synthetic air humidified to various levels of water vapor concentration. These fits also

207   included two other nearby, very weak water lines, with intensities less than 1% of the strong

208   transition, in order that their absorption should not perturb the line shape of the main

209   transition. Results for the shape of the 7816.75210 cm^{-1} line are shown in Figure 4. At the

210   level that we can measure, only the y-parameter has a meaningful variation with water

211   concentration. From the linear fit one obtains a pressure broadening coefficient for air, $\gamma_{air} =$

212   0.0752 cm^{-1}/atm, in reasonable agreement with the Hitran value $\gamma_{air} = 0.0787$ cm^{-1}/atm

213   (Gordon et al., 2017), and a self-broadening coefficient $\gamma_{self} = 0.413$ cm^{-1}/atm, to be compared

214   with the Hitran value $\gamma_{self} = 0.366$ cm^{-1}/atm. Since the uncertainty estimate for the Hitran

215   values is 10 % to 20 %, this level of agreement seems reasonable.

216   We also looked at absorption from water near the Q13Q13 absorption line of O_2.

217   These spectra were measured in a background of pure nitrogen to reveal the very weak lines

218   interfering with the O_2 measurement. Without the strong O_2 lines, it was impossible to

219   interleave FSR-spaced spectra, so in this case the frequency axis comes from the analyzer's

220   wavelength monitor. The upper panel of Figure 5 shows the spectrum of saturated water vapor

221   in nitrogen, together with a fit to a Voigt model of the molecular lines. The measurement was

222   made at a pressure of 340 hPa and temperature of 45° C. The main features are the Q13Q13 line

223   from trace contamination of oxygen in the sample and several lines that arise from normal water

224   ($^1H_2^{16}O$, AFGL code 161) and deuterated water ($^1H^2H^{16}O$, AFGL code 162, also abbreviated HDO). The

225   lower panel of Figure 5 shows the lines tabulated in Hitran. Immediately after the data in

226   Figure 5 were acquired, measurements were also made at 7816.85210 cm^{-1}, to establish the

227   relationship between the absorption strengths in the two spectral regions. The relative

228   intensities of the 161 and 162 lines change with variations in the isotopic composition of the

229   water, but fortunately the direct interference with the oxygen Q13Q13 lines comes entirely

230   from the 161 isotopologue, with the strongest 162 line being separated by approximately 8

231   line widths (FWHM) from the Q13Q13 line. Hitran simulations for molecules other than

232   water that are expected to be present in clean, ambient air indicate that direct interference with

233   the Q13Q13 line should be negligible at the level of precision considered here. In the case of

234   CO_2, the dilution of oxygen due to 400 ppm of CO_2 is significant, and larger than any direct

235   spectral interference.

236   Finally, we investigated the influence of water vapor on the shape of the O_2 Q13Q13

237   line. Switching between the two lasers sources, we acquired FSR-spaced spectra of

238   humidified synthetic air, alternately covering the 7817 cm^{-1} and 7878 cm^{-1} regions. Individual

239   spectra were acquired in less than 2 s, so changes in water vapor concentration between

240   spectra were small. These spectra, with frequency resolution of 0.0206 cm^{-1}, were analyzed by

241   nonlinear least-squares fitting with the following spectral models: the 7817 cm^{-1} spectra were

242   modeled as the sum of an empty-cavity baseline having an adjustable offset level and slope

243   and the water spectrum is modeled with three peaks: one strong line and two weak perturbers.

244   The molecular absorption of the main peak was expressed as an adjustable amplitude, A_w,

245   multiplying a dimensionless, area-normalized Galatry function (Varghese and Hanson, 1984).

246   The weak perturbers were modeled by Voigt profiles with amplitudes and line widths that

247   were constrained to be in fixed proportions to the strong line, and therefore added no new

248   degrees of freedom to the fitting procedure. Since the amplitude A_w multiplies an area-

249   normalized shape function, it is essentially equivalent to the area of the absorption line, to the

250   extent that the Galatry model provides a valid description of the line shape. The Doppler

251   width of the Galatry function was fixed based on the measured cell temperature, the y-

252   parameter was allowed to vary, and the z-parameter was constrained to be proportional to y,

253   based on measurements summarized in Figure 2. In addition, the center frequency of the

254   Galatry function was adjusted to match the data set, giving a total of five free parameters for

255   this fit. The 7878 cm^{-1} spectra were modeled with an adjustable baseline offset and slope and

256   molecular absorption amplitude, A_{O2}, describing the Q13Q13 O_2 line. Here, too, the y-

257   parameter and centration of the O_2 lines were allowed to adjust, and the z-parameter was

258   constrained to be proportional to y. The weak water lines interfering with oxygen absorption

259   were included in the model, but with no additional free parameters; rather the amplitudes were

260   preset based on the measured water absorption at 7817 cm-1 and the previously determined

261   amplitude relationships between the water lines. This procedure does not account for

262   variations in HDO abundance, which may introduce some systematic error into the water

263   vapor correction for samples of unusual isotopic composition, but it should accurately model

264   the most important lines that interfere with the oxygen measurement. Collisional broadening

265   of the Q13Q13 O_2 line by water vapor is shown in Figure 6. From the linear fit one obtains a

266   coefficient for collisional broadening of the Q13Q13 line by water vapor of γ_{water} = 0.0442

267   cm^{-1}/atm. We are not aware of previous measurements of this quantity.

268   The alternating measurements at 7817 cm^{-1} and 7878 cm^{-1} also calibrated the

269   relationship between water mole fraction and the absorption at 7817 cm^{-1}, using a dilution

270   analysis described by Filges et al. (2018), who showed that the results obtained this way agree

271   well with water vapor fractions measured with a conventional hygrometer. Figure 7 shows the

272   measured amplitudes of the water and oxygen lines for samples of variable humidity. Since

273   the air came from a tank of constant composition, the oxygen concentration changes due to

274   dilution of oxygen when water is added. Assuming that this is the sole cause of the change in

275   measured absorption, since the line shapes were being constantly adjusted to account for

276   changes in collisional broadening, it is straightforward to deduce the relation between the

277   water fraction and the absorption amplitude. This calibration was used to generate the water

278   fraction axes in Figures 4 and 6. We note that we did not take particular care to control or

279   measure the quantity of dissolved gases, especially oxygen and carbon dioxide, in the water

280   used for this experiment. While these gases would not significantly affect the water

281   calibration, they may affect the water vapor correction of the oxygen measurement at the ppm

282   level. More work needs to be done to investigate the water vapor correction of the oxygen

283   measurement.

284   The observations described above were used to design a method to measure oxygen

285   concentration in ambient air. Gas from the inlet to the analyzer is drawn through the cavity at

286   a rate of about 100 sccm (standard cubic centimeter per minute) and the conditions in the

287   cavity are held stable at 340 hPa and 45° C. In its analysis mode the analyzer alternately

288   measures ring-downs in the 7817 cm^{-1} and 7878 cm^{-1} regions. At 7878 cm^{-1} measurements are

289   made at 11 different frequencies, spaced by one FSR of the cavity and centered at the peak of

290   the Q13Q13 line. Multiple ring-down measurements are made to improve the precision of the

291   loss determination, with a total of 305 ring-downs allocated to one spectrum. In the 7817 cm^{-}

292   ^{1} region measurements are also made at 11 distinct frequencies at FSR spacings. Only 35 ring-

293   downs are allocated to this spectral region, since the measurement of O_2 is much more

294   important than water vapor. The data sets are analysed using a Levenberg-Marquardt fitting

295   routine, which adjusts five free parameters in each region to find the best agreement to a

296   spectral model based on Galatry line shapes, as described above. One of the outputs of the

297   7878 cm^{-1} fit is the frequency offset of the FSR grid from the center of the Q13Q13 line. This

298   information is used to adjust the position of the PZT actuated mirror to keep the

299   measurements centered on the line, effectively stabilizing the optical path length of the cavity

300   to the frequency of the O_2 line. The reported water fraction is obtained by multiplying the

301   fitted amplitude of the water line by a calibration constant derived from the dilution

302   experiment as explained above. For the O_2 fraction a slightly more complicated procedure is

303   followed. It was observed that the least-squares fitting of the data gives highly correlated

304   results for the amplitude of the absorption line and the line width parameter y. The correlation

305   may be due in part to the fitting procedure itself (Press et al., 1992) and it may also have a

306   contribution from pressure variations that the pressure sensor is unable to detect. The ratio

307   A_{O2}/y can be determined from the fit much more precisely than A_{O2} alone and so gives a more

308   sensitive measurement of molecular absorption. It also has the advantage of being

309   independent of sample pressure, to the extent that the Galatry model applies (Figure 2).

310 However, using the ratio A_{O2}/y as a metric for absorption adds more complications if

311 measurements are to be made over a range of O_2 and water concentrations, because the O_2/N_2

312 ratio and water concentration affect the line width independently of pressure and O_2

313 concentration alone. To minimize systematic errors due to these broadening effects, we define

314 a nominal y-parameter based on the measured amplitudes of the O_2 and water lines and the

315 line broadening dependences shown in Figures 3 and 4. The measured ratio A_{O2}/y is

316 normalized by the nominal y to obtain a quantity that is ideally independent of pressure and

317 water concentration, and this is the quantity that is multiplied by a calibration constant to give

318 the reported O_2 fraction. In addition, a dry mole fraction is reported for O_2, defined as the

319 directly measured mole fraction corrected for water dilution.

320   The main goal in developing this instrument was to make high precision

321 measurements of O_2 mole fraction, based on absorption by the dominant $^{16}O_2$ isotopologue.

322 The absorption lines of the rarer isotopologues are also present nearby, so a mode of operation

323 was included in which one laser is scanned over neighboring lines of $^{16}O_2$ and $^{16}O^{18}O$ and the

324 ratio of amplitudes is used to derive an isotopic ratio, reported in the usual delta notation. In

325 this case the operating pressure was reduced to 160 hPa to improve the resolution of the

326 nearby lines. The lines measured were the Q3Q3 line of $^{16}O_2$, at 7882.18670 cm^{-1}, and the

327 Q9Q9 line of $^{16}O^{18}O$, at 7882.050155 cm^{-1}. The measurement procedure is very much like

328 that for the O_2 fraction measurement, so it will not be described in detail, only the main

329 differences will be noted. One is that in determining an isotopic ratio, normalizing absorption

330 amplitudes to line widths does not provide any advantage, instead we simply take the ratio of

331 amplitudes to compute delta. Although the Q9Q9 line and its neighbor Q8Q8 are the strongest

332 ones in this band, absorption by $^{16}O^{18}O$ is still very weak, only about 5×10^{-9} cm^{-1} at the line

333 center under the conditions we used. Consequently, the signal-to-noise that can be achieved

334 with this analyzer is not adequate to determine both the amplitude and the width of the $^{16}O^{18}O$

335 line with useful precision, so in the fitting step the y-parameter of the $^{16}O^{18}O$ line is

336 constrained to be a constant factor times the fitted y-parameter for the $^{16}O_2$ line. Additionally,

337 because of the weakness of the rare isotopologue absorption, the majority of ring-downs in

338 each spectrum is devoted to measuring $^{16}O^{18}O$ i.e. 232 ring-downs in each spectrum versus

339 only 40 for $^{16}O_2$. This implies that the mole fraction measurement in the isotopic mode is

340 much less precise than when the analyzer measures the Q13Q13 line alone.

341 **3. Results and Discussions**

342 **3.1. Laboratory tests at Picarro, Santa Clara**

343 3.1.1. Temperature and pressure sensitivity

344 One set of tests was done to determine how well the goal was met of minimizing the

345 susceptibility of the concentration measurements to noise or drift of the sample temperature

346 and pressure. For these tests the analyzer sampled dry synthetic air from a tank and the

347 temperature and pressure setpoints of the cavity were adjusted upward and downward from

348 the nominal values, to obtain an estimate of the differential response. We express the

349 sensitivity to experimental conditions in relative form, that is the derivative with respect to

350 temperature or pressure divided by the signal under nominal conditions.

351 From these experiments, we determined a temperature sensitivity of -2.1×10^{-4} K^{-1} and

352 a pressure sensitivity of $+9.8 \times 10^{-6}$ hPa^{-1}. The temperature sensitivity is somewhat larger than

353 expected based on a calculation using Hitran data to estimate the temperature dependences of

354 all the quantities that go into the measured absorption of the Q13Q13 line. The pressure

355 sensitivity is strikingly small, indicating a good cancelation of the pressure dependence of

356 absorption amplitude and line width. Both temperature and pressure sensitivities are small

357 enough to have a negligible effect on short-term precision of measurements made with the

stabilized ring-down cavity, though long-term drifts in the sensors are always a matter of concern.

3.1.2. Measurement precision and drift

Measurement precision was evaluated by analyzing synthetic air containing nominal atmospheric concentrations of CO_2 and CH_4 from an aluminum Luxfer cylinder over a period of several days. The tank, oriented horizontally and thermally insulated (though not controlled), was connected directly to the instrument (S/N TADS2001) with a 2-stage pressure regulator and stainless-steel tubing with an additional orifice to about 55 sccm. For the isotopic mode of operation, the precision of the measurement was also tested by making repeated measurements from a tank of clean, dry synthetic air.

Figure 8 shows the time series of the precision test data, displaying the reported oxygen concentration, the height of the oxygen absorption peak, the width of the oxygen absorption peak and the ambient temperature. The residual error of the analyzer, although small, is nevertheless significant given the stringent targets set forth by the WMO-GAW program. Possible sources of error include: temperature drifts due to sensor drift or gradients; pressure errors due to sensor drift; optical artifacts such as parasitic reflections, higher order cavity mode excitation, and/or loss nonlinearity that can distort the reported oxygen spectrum. More work is required to identify and eliminate these small drifts.

The Allan standard deviation of the reported O_2 fraction is shown in the Allan-Werle plot in Figure 9. The ordinate on this plot is the square root of the Allan variance of reported mole fraction, so 1 ppm in these units corresponds to about 5 per meg in the ratio of O_2/N_2. The precision of averaged measurements improves as $\tau^{-1/2}$ for approximately 5000 s and reaches 1 ppm in less than 10 minutes and remains below 1 ppm for time scales on the order of about 1 hour (Tau is the abscissa of the Allan-Werle plot).

382   Figure 10 shows the precision of $\delta(^{18}O)$ (uncalibrated) derived from the ratio of lines

383   measured at 7882 cm^{-1}. Because of the weak signal from the $^{16}O^{18}O$ line, it is necessary to

384   average for more than 20 seconds or more to achieve 1‰ precision on the isotopic ratio. As

385   for the concentration measurement, averaging improves the measurement precision for time

386   scales up to about 1 hour.

387   **3.2. Laboratory measurements at the University of Bern**

388   3.2.1. Measurements of standard gases

389   The performance of the instrument was tested by analyzing eight standard gases with

390   precisely known CO_2 and O_2 compositions (Table 1) using the CRDS analyzer and comparing

391   it to parallel measurements with a paramagnetic oxygen sensor (PM1155 oxygen transducer,

392   Servomex Ltd, UK) embedded to a commercially available fuel cell oxygen analyzer

393   (OXZILLA II, Sable Systems International, USA) (Sturm et al., 2006) as well as with an

394   isotope ratio mass spectrometer (IRMS, Finnigan Delta^{Plus}XP). The design of the

395   measurement set-up is shown in Figure 11. Standard gases were directly connected to the

396   pressure controlling unit, and a multi-port valve (V2) was used to select among the standard

397   gases. Flow from each cylinder was adjusted to about 120 sccm which was eventually

398   directed to a selection valve (V1), allowing switching between ambient air and standard gases.

399   Flow towards and out of the fuel cell analyzer was controlled by the pressure controlling unit.

400   The O_2 mixing ratio of this incoming gas was first measured on the Paramagnetic O_2 sensor

401   and then directed towards a non-dispersive infrared analyzer (NDIR) (Li-7000, LICOR, USA)

402   for measuring CO_2 and H_2O. The outflow from this analyzer (100 sccm) returns to the

403   pressure controlling unit and was eventually divided between the CRDS analyzer (which uses

404   about 75-80 sccm) and the IRMS (~ 20 sccm) via a Tee-junction. Each cylinder was measured

405   for two hours in each system controlled by a LabView program.

406   First, we investigated the influence of this Tee-junction, which splits the gas flow

407   between the CRDS and the IRMS, on the measured O_2 values. Manning (2001) showed that

408   the fractionation of O_2 in the presence of a Tee-Junction is strongly dependent on the splitting

409   ratios as well as temperature and pressure gradients. Hence, we measured and compared the

410   O_2 mixing ratios of two standard gases (CA07045 and CA060943) in two cases: i) in the

411   presence of a Tee-junction with different CRDS to IRMS splitting ratios and ii) without a

412   Tee-junction so that all gas flow is directed towards the CRDS analyzer. The splitting ratios in

413   these test experiments vary from 1:1 to 1:100, and reversed to change the major flow direction

414   either to the CRDS or the IRMS. Note that the experimental condition in this manuscript is

415   with a 4:1 splitting ratio (i.e. ~ 80 sccm towards the CRDS analyzer and ~ 20 sccm towards

416   the IRMS).

417   In the cases of the smaller splitting ratios (1:1, 1:4 and 4:1), which are relevant for the

418   results presented in this study, only minor differences in the measured O_2 mixing ratios were

419   observed when compared to case ii (i.e. without a Tee-junction). For these two cylinders

420   measured, the average differences in these cases were about 0.5 ppm, calculated as the mean

421   of the differences in the raw O_2 measurements of the last 60 seconds. The negligible

422   fractionation can indeed be the result of smaller splitting ratios while strong influence is

423   usually expected in case of larger splitting ratios (Stephens et al., 2007). For higher splitting

424   ratios, the result seems inconclusive without any dependence on the ratios due to the strong

425   decline in the cylinder temperature (specifically at the pressure gauge) caused by higher flow

426   to achieve the higher splitting ratios (as high as 1:100). Hence, these tests need to be

427   conducted in a temperature-controlled condition and the results could not be discussed in this

428   manuscript.

Figure 12 shows the standard gas measurements for the seven cylinders with known CO_2 and O_2 mixing ratios (Table 1) using both the CRDS and the Paramagnetic analyzers. Standard eight, which has too high O_2, is not shown in the figure as the figure is zoomed-in to better illustrate the change in O_2 for the remaining cylinders. While the first five cylinders contain O_2 and CO_2 mole fractions comparable to ambient air values, standards 6 & 8 had either very low or very high O_2, respectively. In addition, standards 6 and 7 have very low and very high CO_2 mixing ratios. Note that due to its very high CO_2 content ($\sim$ 2700 ppm), standard 7 was not measured on the IRMS and hence the O_2 mixing ratio is unknown. The measured mixing ratios for the six standard gases measured with the two systems are in very good agreement while cylinder 7 showed an opposing signal for the two analyzers compared to standard 6 (Figure 12). While the Paramagnetic analyzer showed a higher O_2 mixing ratio, the values from the CRDS analyzer are lower in O_2. This can be associated with the very high CO_2 mixing ratio in standard 7, which leads to a strong dilution effect in the CRDS analyzer as it does not include any correction function for dilution effect from CO_2. However, such high CO_2 mixing ratios may not be that important for most atmospheric research. Yet, it should be considered to include a parallel CO_2 mixing ratios measurement to the instrument as it will further improve the accuracy. This would be especially important for biological or physiological studies where a wide range of CO_2 and O_2 concentrations must be expected.

The measurement precision of the CRDS analyzer was calculated as the standard error of the mean i.e. the standard deviation (1-σ) of the last 1-minute raw measurements divided by the square root of the number of measurements (n = 60), and for all these cylinders the values are usually between 0.5 ppm to 0.7 ppm. For parallel measurements of these cylinders using a Paramagnetic analyzer, we obtained a precision of about 1 ppm, calculated exactly the same way.

453   We also made a correlation plot to see which of the two instruments are in better

454   agreement with the assigned values based on IRMS measurements for the individual

455   cylinders. While similar correlation coefficients were observed for both analyzers, different

456   slopes were calculated (Fig. A.1). This is due to the fact that the IRMS measures the O_2 to N_2

457   ratio ($\delta(O_2/N_2)$) in per meg, while the CRDS and the Paramagnetic analyzers provide non-

458   calibrated O_2 mixing ratios in units of ppm and per meg, respectively. If we exclude the two

459   standard gases with the highest and lowest O_2 mixing ratios (standards 7 and 8) that are

460   subjected to strong dilution effects, both the slope and the r^2 values decrease from those

461   shown in Figure A.1. But this decrease is larger in the case of the Paramagnetic

462   measurements, implying a slightly better linearity of the CRDS analyzer.

463   3.2.2. Measurements of ambient air

464   Ambient air measurements were conducted from the roof top of our laboratory at the

465   University of Bern to evaluate the analyzer's performance under atmospheric variability.

466   Ambient air was continuously aspirated from the inlet at the roof of the building at a flow rate

467   of ~ 250 sccm which is then dried using a cooling trap kept at -90 °C towards the switching

468   valve (V1) and measured in similar way to the standard gases as explained above. The

469   measurement values obtained here were compared with the parallel measurements by the

470   Paramagnetic sensor to test the instruments stability and accuracy.

471   Figures 13 panels a &b show the 1-minute average ambient air measurements from the

472   rooftop inlet by the Paramagnetic and the CRDS analyzers at the beginning of the testing

473   period including standard gases measured every 12-hour. While the Paramagnetic analyzer

474   seems to be stable, the CRDS analyzer showed a strong drift for an extended period. This can

475   be due to unstable conditions in the CRDS measurement system as it started operating right

476   after it was unpacked. Hence, we looked into temperature inside the instrument chassis and

pressure records, which were stable within the manufacturer's recommended range during this period. As the CRDS analyzer incorporates a water correction function, interference from this species should be well accounted. Even comparing the analyzer's parallel water measurements to water measurements by the NDIR system such a drift was not observed. It should be noted that the two internal standard gases which were less frequently measured (every 12 hours) during this period were also drifting following similar pattern. This implies that the drift is associated with the analyzer. Interestingly, this pattern can be modeled using a polynomial function which can then be used to correct for the observed drift in the ambient air measurements. After applying a polynomial drift correction, we were able to fully accounted for the observed drift. However, the manufacturer decided to further investigate possible causes of this drift. After further improvements, we obtained the first commercial analyzer in September 2017 and repeated the above tests (Figure 13 c &d). No such drift was observed any more in the standard gases or in ambient air measurements.

We believe that the optical amplifier has caused the drift in the first system and not anymore included in the design of the product which produced a significant amount of broadband light that could fill the cavity (albeit with a low coupling coefficient), and would ring down with a different (and generally much faster) time constant that the baseline loss of the cavity. However, the ringdown time on the peak of the oxygen line is just 10 microseconds, such that the broadband light might have distorted the single exponential decay of the central laser frequency, leading to the observed drift in the oxygen signal. However, we were not able to confirm this hypothesis.

3.2.3. Water correction test

Measurements of oxygen are reported as both wet ($O_{2, \text{raw}}$) and dry ($O_{2, \text{dry}}$) mole fractions by the CRDS analyzer as it also measures water vapor in parallel at its water

501 absorption line (7817 cm^{-1}), and corrects for the dilution effect based on an inbuilt numerical

502 function:

503
$$O_{2,dry} = \frac{O_{2,raw}}{1 - f_{H_2O}} \qquad (5)$$

504 where f_{H2O} is the measured water mole fraction.

505 The efficiency of water correction by this function was assessed in two ways: i) by comparing

506 the water vapor content in standard air measured by this analyzer with similar measurements

507 by the NDIR analyzer and ii) by comparing the oxygen mixing ratios between non-dried

508 ambient air measured and corrected for water dilution by the CRDS analyzer with dried air

509 measured using a paramagnetic analyzer.

510 Figure 14 shows the water vapor content for standard gases measured continuously for

511 two days by the CRDS and the NDIR analyzers. Note that the two data sets are manually

512 fitted to each other as the measured water values by the NDIR analyzer are not calibrated.

513 Based on this plot, the two analyzers are in very good agreement although there are small

514 differences during very dry conditions (low water content).

515 Figure 15a shows the dried ambient air water measurements in both analyzers with

516 frequent spikes due to valve switching while measuring standard gases. In the second case,

517 where the water trap was by-passed and non-dried air was allowed to the CRDS analyzer

518 keeping the dried air flow to the NDIR (Figure 15b), a clear increase in the water

519 measurements in the CRDS analyzer can be observed. Here, it should be noted that there are

520 no spikes in the water measurements of the CRDS analyzers as there are no standard gas

521 measurements in between and the inlet is directly connected to the CRDS analyzer (Figure

522 11). Figures 15c & 15d show the difference in oxygen measurements of ambient air measured

523 in both analyzers in the two cases stated above (note that the CRDS uses its built-in water

correction function applying Eq. 5). The measurements of the Paramagnetic analyzer were scaled to ppm units by applying the correlation equation obtained from the six standard gas measurements of the two analyzers (Fig. A.1). Note that the CRDS measurements were corrected for the observed drift using the polynomial fit to the two standard gas measurements stated above.

In the first period of the measurement when both analyzers measured dried ambient air, the absolute differences between the 1-minute averages measured over two days by the two analyzers were mostly within 15 ppm (Figure 15c) and symmetrically distributed around zero (Figure 15e). However, when wet air was admitted to the CRDS analyzer and the in-built water correction was applied, a stronger variability was observed in the calculated differences (Figure 15d). This implies stronger short term variability in the CRDS analyzer measurement values (as nothing was changed for the Paramagnetic measurement system) when wet samples were analyzed. The more negative values in the differences (Figure 15f) can also be associated with overestimation of the O_2 mixing ratios by the CRDS originating from an overestimated water correction. However, detailed evaluation of the analyzer's water correction function is beyond the scope of this study.

3.3. Field Measurements

After a series of tests at University of Bern, we conducted multiple field measurements at the High Altitude Research Station Jungfraujoch and the Beromünster tall tower sites in Switzerland described below.

3.3.1. Tests at the High Altitude Research station Jungfraujoch

The High Alpine research station Jungfraujoch is located on the northern ridge of the Swiss Alps (46° 33′ N, 7° 59′ E) at an elevation of 3580 m a.s.l. It is one of the global atmospheric watch (GAW) stations well-equipped for measurements of numerous species and

548   aerosols. The site is above the planetary boundary layer most of the time due to its high

549   elevation (Henne et al., 2010; Zellweger et al., 2003). However, thermally uplifted air from

550   the surrounding valleys during hot summer days or polluted air from the heavily industrialized

551   northern Italy may reach at this site (Zellweger et al., 2003). The Division of Climate and

552   Environmental Physics at the University of Bern has been monitoring CO_2 and O_2 mixing

553   ratios at this site based on weekly flask sampling and continuous measurements since 2000

554   and 2004, respectively (Schibig et al., 2015). The CO_2 mixing ratio is measured using a

555   commercial NDIR analyzer (S710 UNOR, SICK MAIHAK) while O_2 is measured using the

556   Paramagnetic sensor (PM1155 oxygen transducer, Servomex Ltd, UK) and fuel cells (Max-

557   250, Maxtec, USA) installed inside a home-built controlling unit. Similar to the comparison

558   tests at the University of Bern, we have conducted parallel measurements between the CRDS

559   analyzer and the paramagnetic cell at this high altitude site during 03 – 14 February 2017. The

560   measurement of ambient air at the Jungfraujoch system is composed of sequential switching

561   between low span (LS) and high span (HS) calibration gases followed by a target gas (T)

562   measurement (once a day) to evaluate the overall system performance and finally a working

563   gas (WG) measurement before switching back to ambient air.

564   Figure 16 (top panel) shows the calibrated 1-minute averaged O_2 mixing ratios

565   measured at this high altitude site in comparison with the Paramagnetic oxygen analyzer

566   already available at the site. Despite the strong variability observed during the measurement

567   period of 10-days by both analyzers, a very good agreement was observed between them.

568   Figure 16 (bottom panel) shows the absolute difference of 1-minute averages in

569   atmospheric O_2 measured at Jungfraujoch between the two analyzers which are mostly within

570   ±5 ppm range (but sometimes going as high as ±10 ppm) without an offset. However, for

571   generally reported 10-minutes, half-hourly or hourly means these values correspond to < 1.5

572   ppm, < 1 ppm and < 0.65 ppm.

573   3.3.2. Tests at the Beromünster tall tower site

574   The Beromünster tower is located near the southern border of the Swiss Plateau, the

575   comparatively flat part of Switzerland between the Alps in the south and the Jura mountains

576   in the northwest (47° 11′ 23″ N, 8° 10' 32″ E, 797 m a.s.l.), which is characterized by intense

577   agriculture and rather high population density. A detailed description of the tower

578   measurement system as well as a characterization of the site with respect to local

579   meteorological conditions, seasonal and diurnal variations of greenhouse gases, and regional

580   representativeness can be obtained from previous publications (Berhanu et al., 2016; Berhanu

581   et al., 2017; Oney et al., 2015; Satar et al., 2016). The tower is 217.5 m tall with access to five

582   sampling heights (12.5 m, 44.6 m, 71.5 m, 131.6 m, 212.5 m) for measuring CO, CO_2, CH_4

583   and H_2O using Cavity Ring Down Spectroscopy (Picarro Inc., G-2401). By sequentially

584   switching from the highest to the lowest level, mixing ratios of these trace gases were

585   recorded continuously for three minutes per height, but only the last 60 seconds were retained

586   for data analysis. The calibration procedure for ambient air includes measurements of

587   reference gases with high and low mixing ratios traceable to international standards (WMO-

588   X2007 for CO_2 and WMO-X2004 for CO and CH_4), as well as target gas and more frequent

589   working gas determinations to ensure the quality of the measurement system. From two years

590   of data a long-term reproducibility of 2.79 ppb, 0.05 ppm, and 0.29 ppb for CO, CO_2 and

591   CH_4, respectively was determined for this system (Berhanu et al., 2016).

592   Between 15.02.2017 and 02.03.2017, we have connected the new CRDS oxygen

593   analyzer in series with the CO_2 analyzer (Picarro G-2401) and measured the O_2 mixing ratios

594   at the corresponding heights. Similar to the CO_2 measurements, O_2 was also measured for

595 three minutes at each height. During this period, we have evaluated the two features (isotopic

596 mode and concentration mode) of the CRDS analyzer. In the isotopic mode, the CRDS

597 measures the $\delta^{18}O$ values as well as the O_2 concentration while in concentration mode only

598 the latter was measured.

599 During the tests conducted at this tower site, we first evaluated the two operational

600 modes (concentration vs isotopic modes) of the CRDS analyzer. Ambient air measurements

601 on isotopic mode over a 4-days period showed a strong variability in the measured oxygen

602 mixing ratios and it was not possible to distinguish the variability in the O_2 mixing ratios

603 among the five height levels. The calculated 1-minute standard error for ambient air

604 measurements was as high as 10 ppm while a standard error of less than 1 ppm was

605 determined from similar measurements in the concentration mode. Additionally, comparing

606 the O_2 values between the two modes, frequent short time variation in ambient air O_2 (~ 200

607 ppm) was observed in the isotope mode measurements while the variation in the concentration

608 mode is significantly smaller (~ 30 ppm). This precision degradation is due to the weaker ^{16}O

609 oxygen line used for the isotopic mode, and the fact that far more ring-downs are collected on

610 the rare isotopologue in isotopic mode Hence, we have conducted the remaining test

611 measurements in concentration mode.

612 As this tower has five sampling height levels, we first followed three minutes of

613 switching per inlet level, which enables four measurements per hour at a given level.

614 However, we noticed hardly any difference among the different levels due to strong short

615 term variability in O_2 mixing ratios between the consecutive heights. Hence, we switched to a

616 longer sampling period of six-minutes per height. Figure 17 shows the diurnal CO_2 and O_2

617 variations at the lowest (12 m) and highest (212.5 m) sampling heights of the tower. These

618 two heights were selected simply to better illustrate the difference in the mixing ratios. The

619 CO_2 mixing ratios on the top panel show higher values at the 12 m inlet than the highest level

620 most of the day due to its closeness to sources except during the afternoon (11:00 - 17:00

621 UTC) when both levels show similar but decreasing CO_2 mixing ratios. This is due to

622 presence of a well-mixed planetary boundary layer (PBL) (Satar et al., 2016). The lag in CO_2

623 peak between the two height levels by about two hours indicates the duration for uniform

624 vertical mixing along the tower during winter 2017. The opposite variability patterns are also

625 clearly visible in the O_2 mixing ratios shown in the lower panel with a clear distinction

626 between the two height levels during early in the morning and in the evening while similar O_2

627 values were observed in the afternoon. These opposing profiles are expected as CO_2 and O_2

628 are linearly coupled with a mean oxidation ratio of -1.1 ± 0.05 (Severinghaus, 1995) for land-

629 biospheric processes (photosynthesis and respiration) and -1.44 ± 0.03 for fossil fuel burning

630 (Keeling, 1988b).

631 Table 2 shows the oxidation ratios derived as the slopes of the linear regression

632 between CO_2 and O_2 mixing ratios at the different height levels measured on 25 February

633 2017. Accordingly, height dependent slopes were observed with a slope of -0.98 ± 0.06 at the

634 lowest level, close to the biological processes induced slope but slightly lower than its mean

635 value. For the highest level, we calculated a slope of -1.60 ± 0.07 a value close to fossil fuel

636 combustion oxidation ratio. Note that depending on fossil fuel type the oxidation ratio can

637 range between -1.17 and -1.95 for coal and natural gas, respectively (Keeling, 1988b). While

638 the slopes derived for the two other levels (44.6 m and 131.6 m) show similar values between

639 the highest and lowest height levels, possibly from mixed sources, the middle level showed a

640 slightly higher slope than these two levels but still in the large range between the lowest and

641 highest inlet heights.

642 3.4. Evaluation of the $\delta^{18}O$ measurements

643   To further evaluate the analyzer's performance in measuring stable oxygen isotopes,

644   we conducted ambient air isotopic composition measurements as well as analyzed a standard

645   gas without CO_2 which has a known $\delta^{18}O$ value. The choice of this CO_2-free air standard gas

646   is twofold: one it has a known $\delta^{18}O$ value and second as it has no interference from possible

647   CO_2 absorption band overlap. For this test three 0.5 L glass flasks were preconditioned and

648   filled with this standard gas to ambient pressure. These flasks were attached before or after

649   the water trap (Fig. 11) and measured similar to ambient air measurements. These

650   measurements were then compared with $\delta(^{34}O/^{32}O)$ values obtained by parallel measurements

651   using our IRMS.

652   Figure 18 shows the $\delta^{18}O$ values of ambient air from the roof top with three

653   consecutive measurements of glass flasks filled with CO_2-free air in-between followed by a

654   fourth flask filled with breath air. An excellent agreement was observed for measurements

655   from both instruments for the three flasks filled with a standard gas. However, the fourth flask

656   with breath air showed a signal opposite to the measurements by the IRMS. As breath air

657   contains large amount of water and CO_2 in addition to O_2, which can possibly interfere with

658   the CRDS analyzer measurements, we have removed H_2O and CO_2 by using a cryogenic trap

659   (-130 °C) and in an additional experiment using Schütze reagent to remove both CO and CO_2.

660   However, we have not observed any improvement towards an agreement with the IRMS

661   measurements. Therefore, any other gas component in the breath air must be relevant for the

662   interference. Based on the absorption lines in the spectral range of the instrument (7878 cm^{-1})

663   retrieved from HITRAN database, we expect interference either from carbon monoxide (now

664   excluded by the tests) or methane or VOCs including acetone, ethanol, methanol or isoprenes,

665   all of which have been measured in breath air (Gao et al., 2017; Gottlieb et al., 2017; Mckay

666   et al., 1985; Ryter and Choi, 2013; Wolf et al., 2017). Further investigations have to shed light

667   on these interferences in order to take corresponding action to surpass these shortcomings in

668   the isotope analysis based on cavity ring-down spectroscopy.

4. Conclusions

670   We have thoroughly evaluated the performance of a new CRDS analyzer which

671   measures O_2 mixing ratios and isotopic composition combining laboratory and field tests.

672   Even if a drift in the analyzer was observed at the beginning of this study, which can be easily

673   corrected by calibration, the recent analyzers built by the manufacturer did not show such

674   instrumental drift. However, prior tests are recommended to see the analyzer's stability.

675   The T-split tests for the current measurement setup based on the measurements of two

676   standard gases showed a difference within the measurement uncertainty. However, this effect

677   may become significant while applying larger splitting ratios and we recommend conducting

678   further experiments to accurately quantify this influence for larger splitting ratios.

679   We have observed a strong influence of dilution in the measured O_2 values during the

680   presence of high CO_2 mixing ratios. Even if such an influence may not be critical for the

681   present study, such an effect might be significant in other studies where higher CO_2 mixing

682   ratios might be present and we recommend following a correction strategy based on parallel

683   CO_2 measurements. This also applies for more accurate analysis.

684   The water correction applied by the instrument's in-built function seems to sufficiently

685   correct for the water vapor influence. However, a larger variability of the difference was

686   observed between the CRDS analyzer and the Paramagnetic cell when dried samples were

687   used in both systems. This can possibly be due to an overcorrection by the water correction

688   function of the CRDS analyzer when dried samples were used. This is particularly true for the

689   very low water vapor range (< 100 ppm). We believe that it is important to further investigate

690   this issue and identify an improved water correction strategy.

Based on the analysis of O_2 mixing ratios in the concentration and isotopic modes, we have observed a significant decrease in precision (about ten-fold) in the latter measurement mode. The measured $\delta^{18}O$ values for the standard air by the CRDS analyzer are in excellent agreement with the IRMS values. However, such measurements for a breath air showed a contrasting signal, possibly due to interference from other gases such as CH_4. Hence, we recommend further investigation on such possible contaminants and how to possibly remove them while conducting ambient air measurements. However, we believe that this analyzer can be used for tracer experiments where artificially enriched isotopes are used to study biological processes such as photosynthesis in plants using isotopically labelled CO_2 and H_2O.

Acknowledgement

We would like to thank ICOS-RI and the Swiss National Science Foundation (SNF) for funding ICOS-CH (20FI21_148994, 20FI21_148992). We are also grateful to the International Foundation High Alpine Research Stations Jungfraujoch and Gornergrat. The measurement system at the Beromünster tower was built and maintained by the CarboCount-CH (CRSII2_136273) and IsoCEP (200020_172550) projects both funded by SNF.

Table 1. Assigned mixing ratios of standard gases used in this study and their corresponding values measured by the NDIR, CRDS and IRMS at the University of Bern. [1]The assigned values are based on measurements from different institutions (University of Bern (UB), Scripps or NOAA, see column cylinder name). [2]Measurements are on the Bern scale for CO_2 and O_2. The Bern scale is shifted by +550 per meg. [3]Values on the Scripps scale.

Cylinder name	Assigned CO_2 (ppm) [1]	Assigned O_2 (per meg) [1]	CO_2-IRMS (ppm) [2]	CO_2-NDIR (ppm) [2]	O_2-IRMS (per meg) [2]	O_2-Paramagnetic (per meg) [2]	O_2-CRDS (per meg) [2]
ST-1 LUX3576-UB	427.47	-1026	427.47	427.59	-1026	-1070	-1057
ST-2 LK922131-UB	368.09	599	368.09	367.82	599	560	590
ST-3 CA07045-Scripps	382.303	-271.6	382.50	381.99	278 (-272.2)[3]	302	281
ST-4 CA07043-Scripps	390.528	-476.4	390.69	390.15	71 (-479.5)[3]	66	63
ST-5 CA07047-Scripps	374.480	-807.7	374.70	374.17	-253 (-803.3)[3]	-212	-233
ST-6 CA04556-NOAA	192.44	-3410	191.21	191.64	-3410	-2905	-3013
ST-7 CA06943-	2699.45	-		2612.80	-	-2691	-3369

NOAA						
ST-8 LK76852-UB	411.49	37794	411.49	406.25	37794	34513	36017

722

723

Table 2. The CO_2 and O_2 correlation coefficients at the different height levels derived using the least square fit and the correlation coefficients (r^2). Uncertainties are calculated as standard error of the slope.

Height	Oxidation Ratios (O_2:CO_2)
12.5 m	-0.98 ± 0.06 (0.48)
44.6 m	-1.29 ± 0.07 (0.50)
71.5 m	-1.49 ± 0.08 (0.47)
131.6 m	-1.23 ± 0.05 (0.55)
212.5 m	-1.60 ± 0.07 (0.61)

727

728

729

730

731

732

733

734
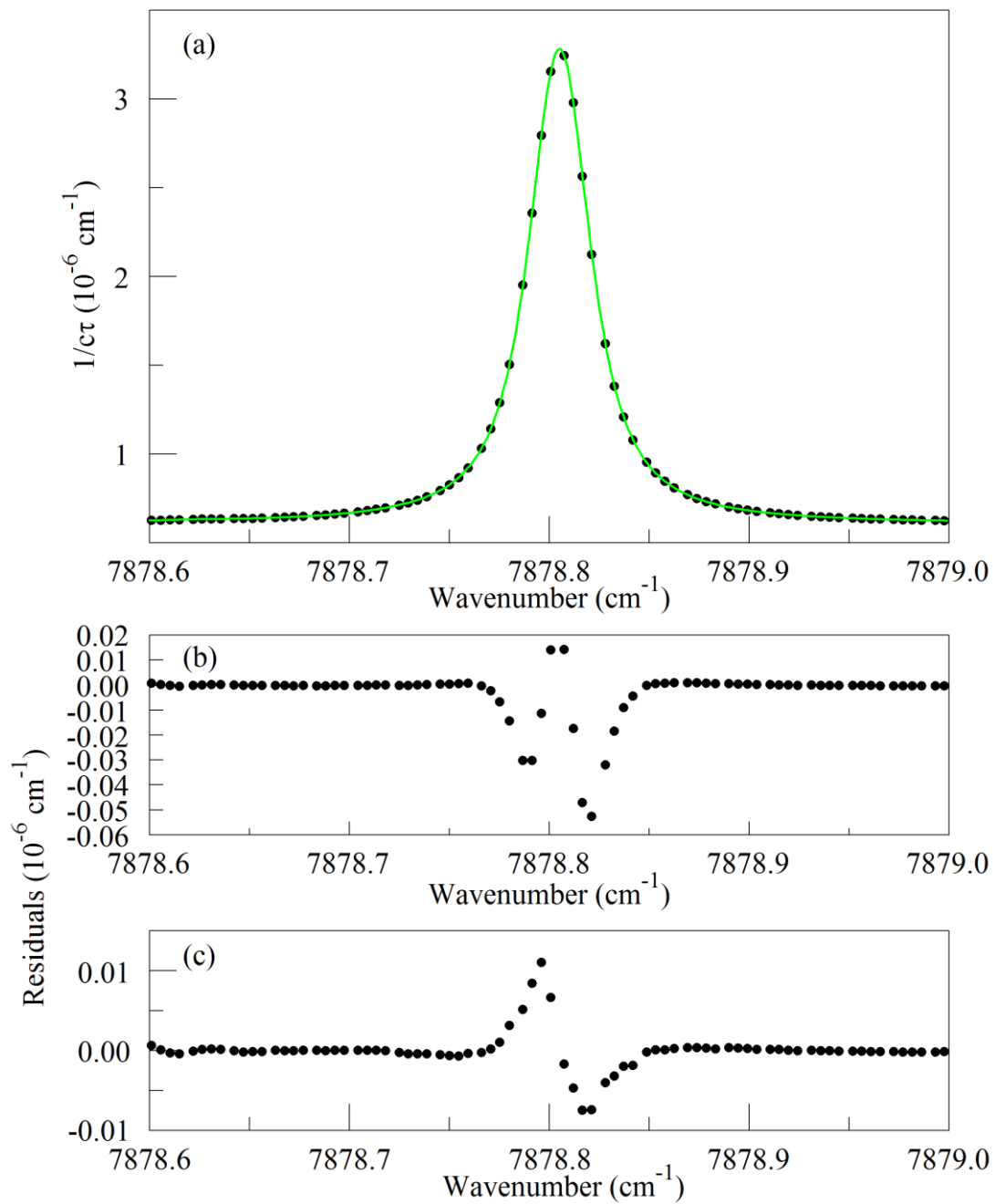
736

737   Figure 1. The top panel (a) shows the raw data (points) and the best-fit Galatry function (solid

738   line). Residuals of the Voigt fit are shown in panel (b) and residuals of the Galatry fit are

739   shown in panel (c).

740

741
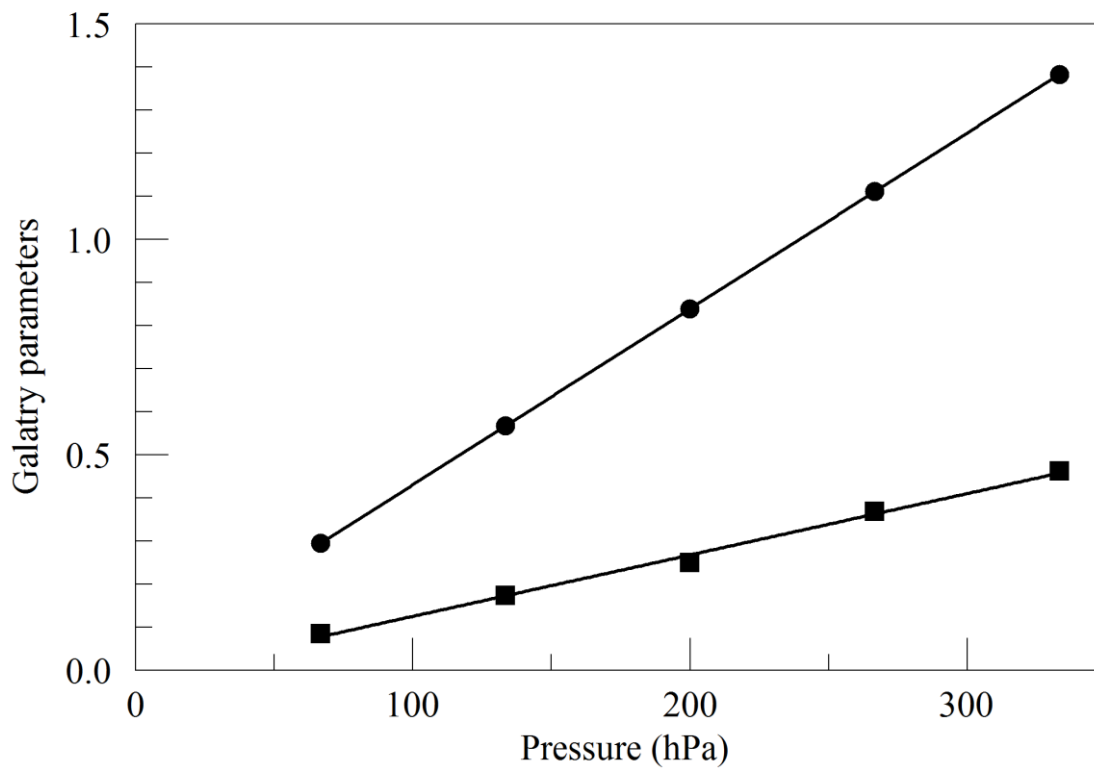
742

743   Figure 2. Best-fit values for the Galatry parameters of the Q13Q13 line of O_2, as a function of

744   pressure. The line broadening parameter y is represented by circles and the line narrowing

745   parameter z by squares. The solid lines are linear fits to the measurements. The best-fit offset

746   and slope are 0.0227 and 0.004082 hPa^{-1} for y, and -0.0169 and 0.001424 hPa^{-1} for z.
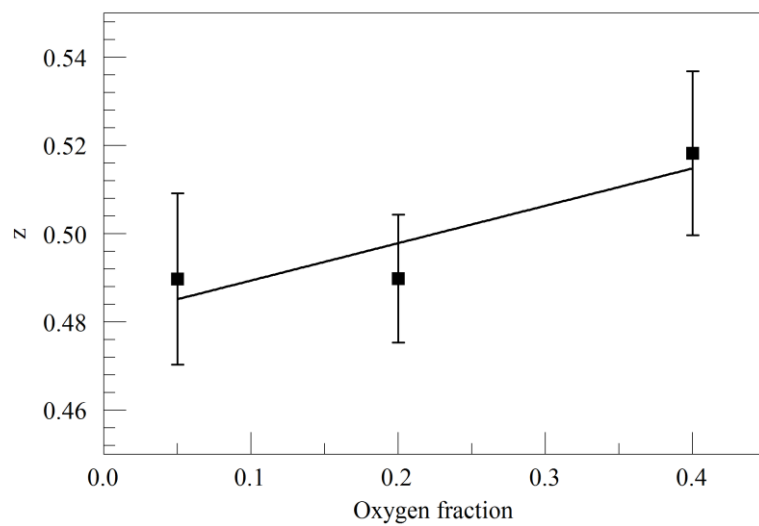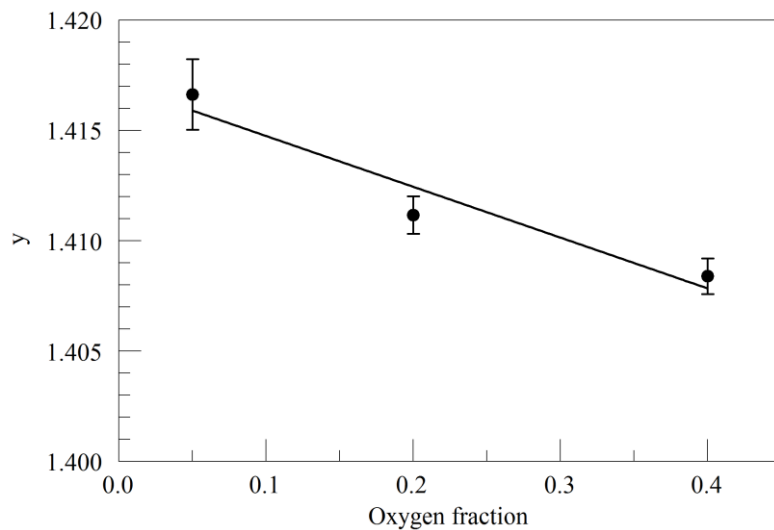
747

748   Figure 3. Galatry parameters of the Q13Q13 line of O_2 at 340 hPa and 45° C as a function of

749   O_2 mole fraction in binary O_2 - N_2 mixtures. The linear fits to the data are y = 1.417 – 0.023 x

750   f_{O2} and z = 0.481 + 0.085 x f_{O2}.
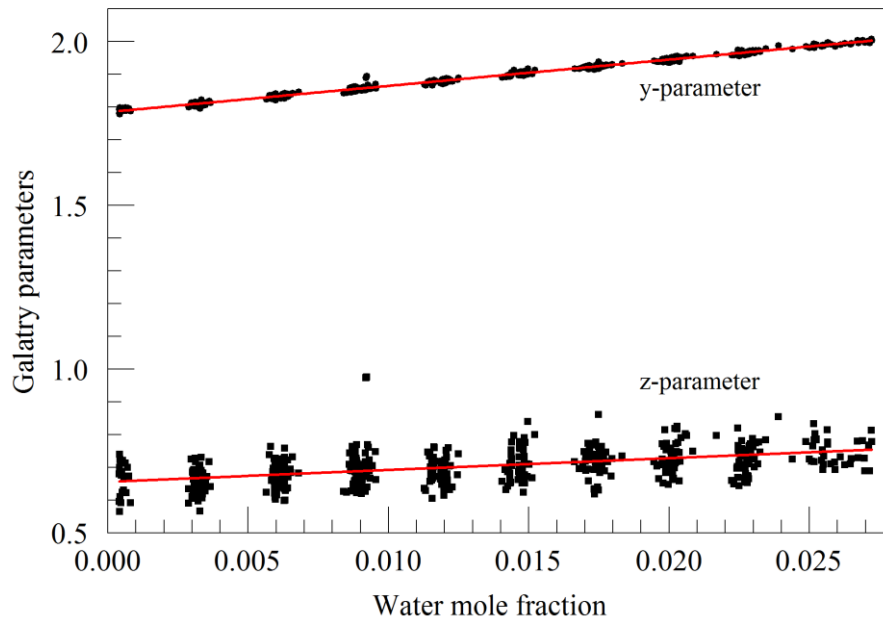
751

752 Figure 4. Galatry parameters of the 7816.75210 cm^{-1} water line in air at 340 hPa and 45° C as

753 a function of water mole fraction. Black points are from measurements and red lines are

754 linear fits: $y = 1.7846 + 8.01 \times f_{H2O}$ and $z = 0.656 + 3.60 \times f_{H2O}$.

755

756

757
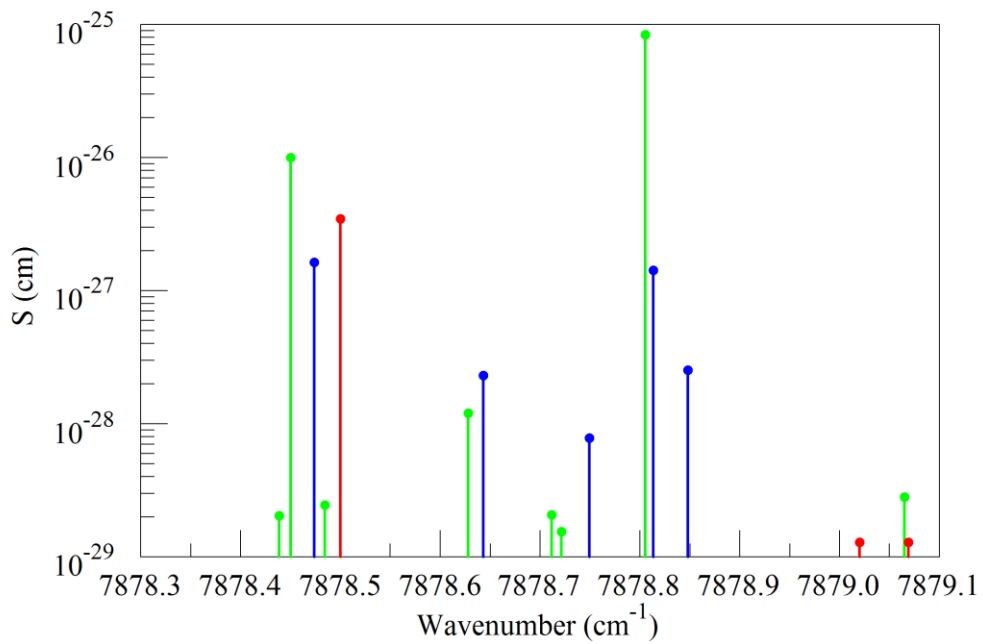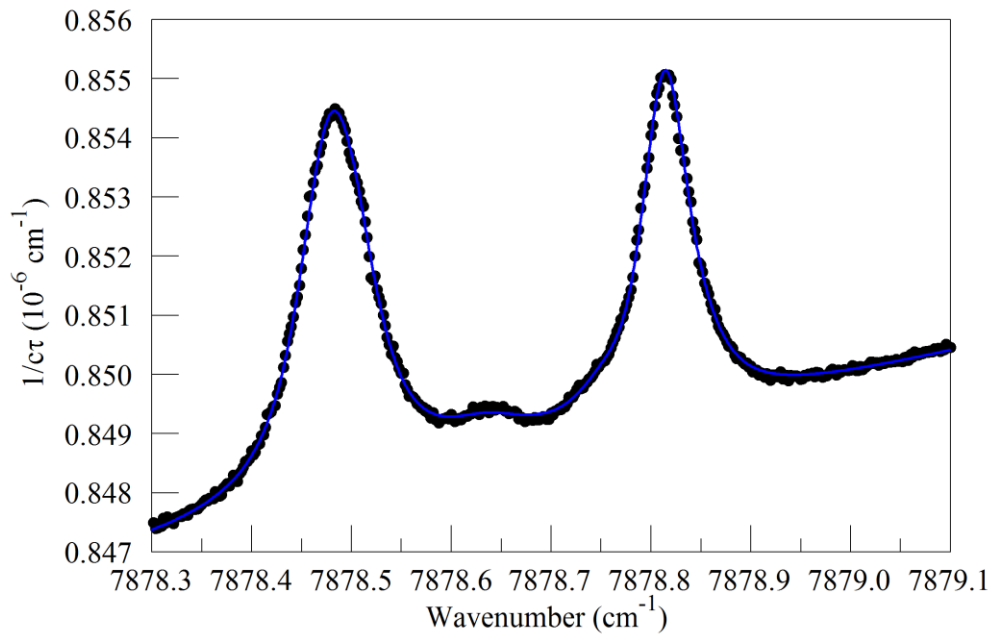
758

759   Figure 5.   Upper panel: spectrum of water in nitrogen (points) and fit to Voigt model (blue

760   curve).   Lower panel: Oxygen (green), normal water (blue), and deuterated water (red) lines

761   in the 2016 Hitran data base.

762

763
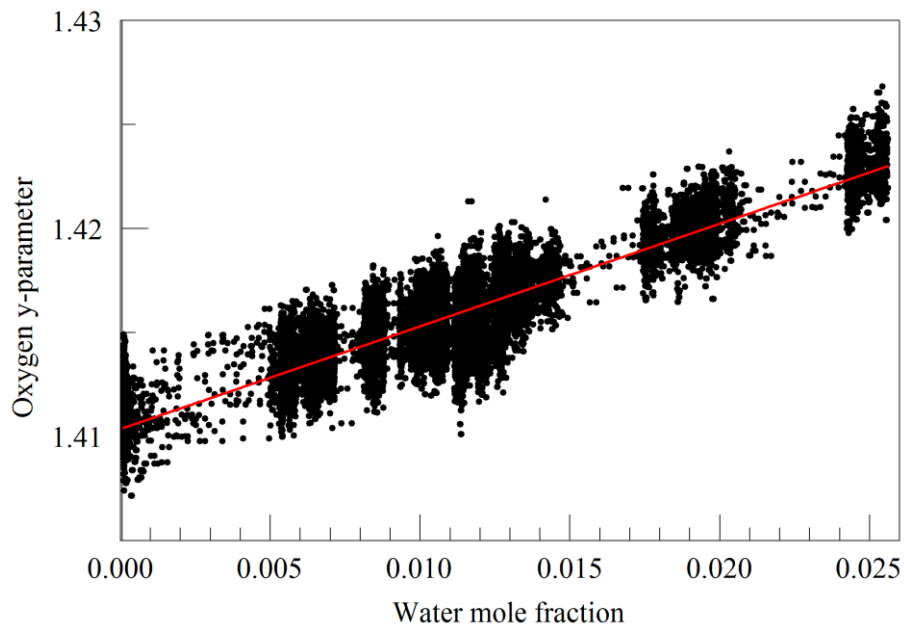
764

765   Figure 6. Galatry collisional broadening parameter of the oxygen Q13Q13 line at 340 hPa

766   and 45° C versus water mole fraction. Black points are from measurements and the red line is

767   a linear fit: $y = 1.4109 + 0.467\ f_{H2O}$.

768

769

770
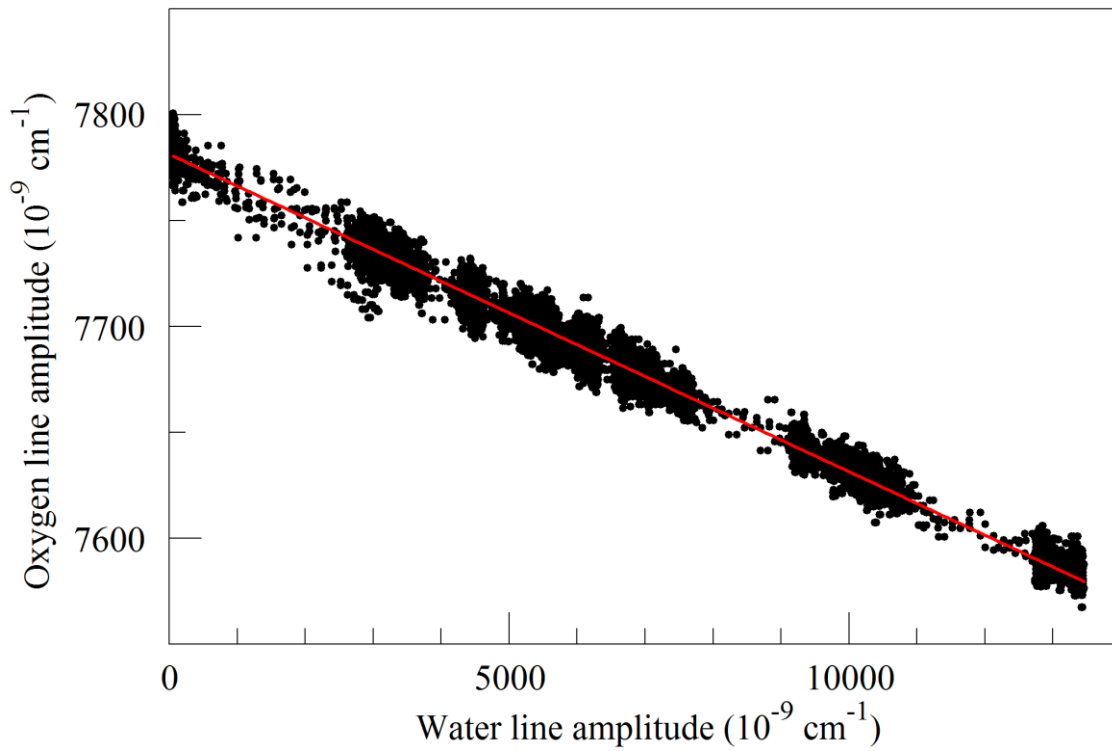
771

772   Figure 7. Measured absorption line amplitudes for oxygen and water vapor for water vapor

773   mixing ratios ranging from nearly 0 to 0.025. Black points are from measurements and the

774   red line is a linear fit: with intercept 7.78001×10^{-6} cm^{-1} and slope -0.014807.

775

776

777

778

779

780
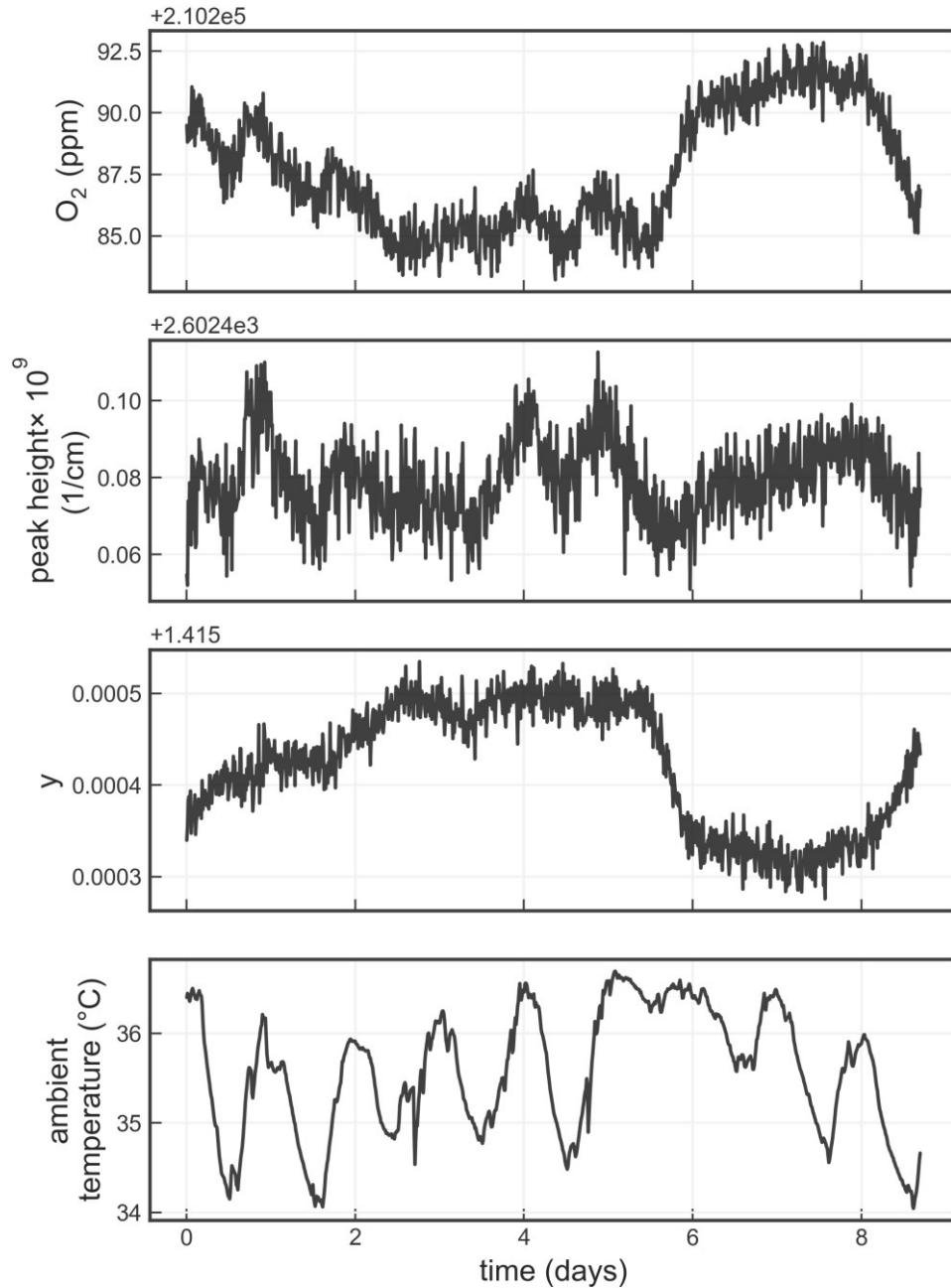
Figure 8. Time series from a measurement of a single tank over about a week. The four panels show the water-corrected oxygen concentration, the absorption peak loss minus the baseline loss, the measured Lorentzian broadening factor, and the ambient temperature (measured in the instrument housing), respectively. A windowed average of 300 seconds was applied to all four data sets.
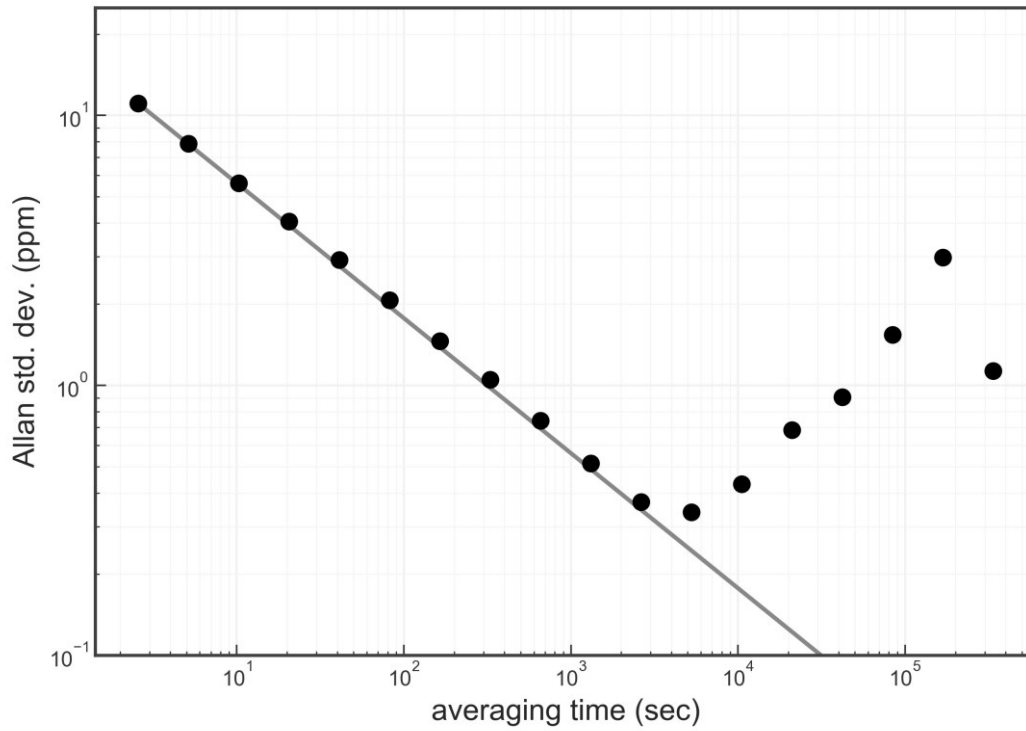
787

788 Figure 9. Precision of O_2 mole fraction measured from a tank of synthetic air. Filled circles

789 are measurements and the line shows the ideal $\tau^{-1/2}$ dependence.

790

791

792

793

794

795
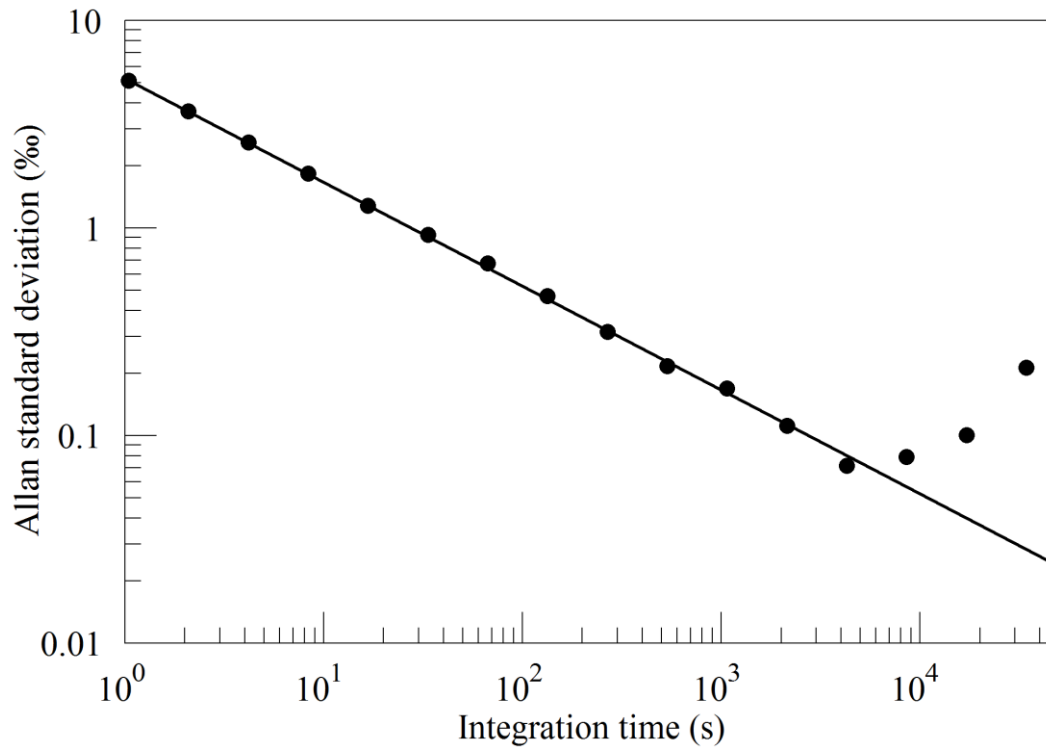
Figure 10. Precision of δ(^{18}O) measured from a tank of synthetic air. Filled circles are

796

measurements and the line shows the ideal $\tau^{-1/2}$ dependence.

797

798

799

800

801

802

803

804

805
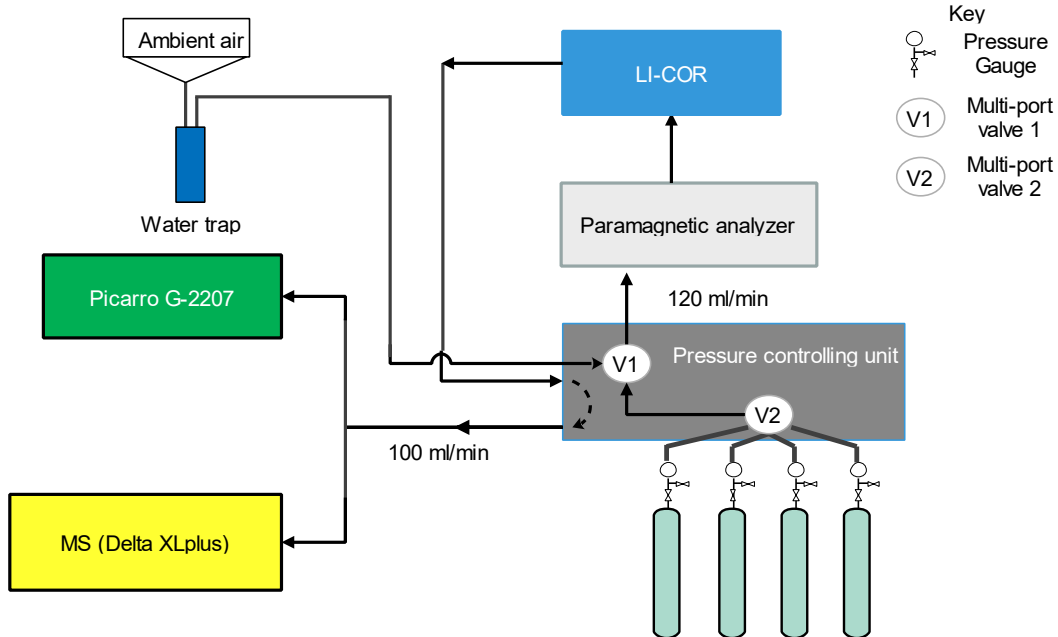
806

807 Figure 11. Schematics of the measurement system used to compare the Picarro analyzer with

808 the Mass Spectrometer at Bern.

809

810

811

812

813

814

815

816

817
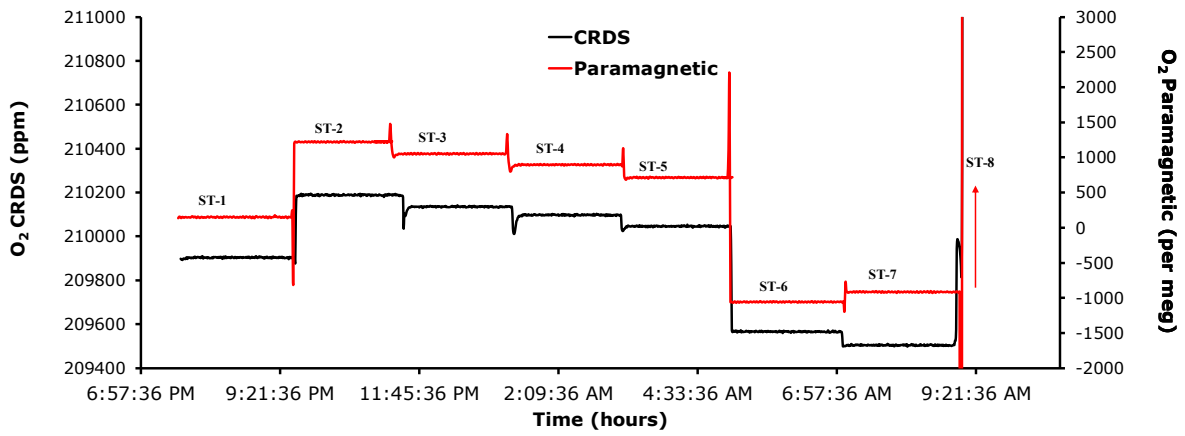
Figure 12. Comparison of oxygen mixing ratios for the seven standard gases measured using the CRDS analyzer (black) and the Paramagnetic sensors (red).

836

837
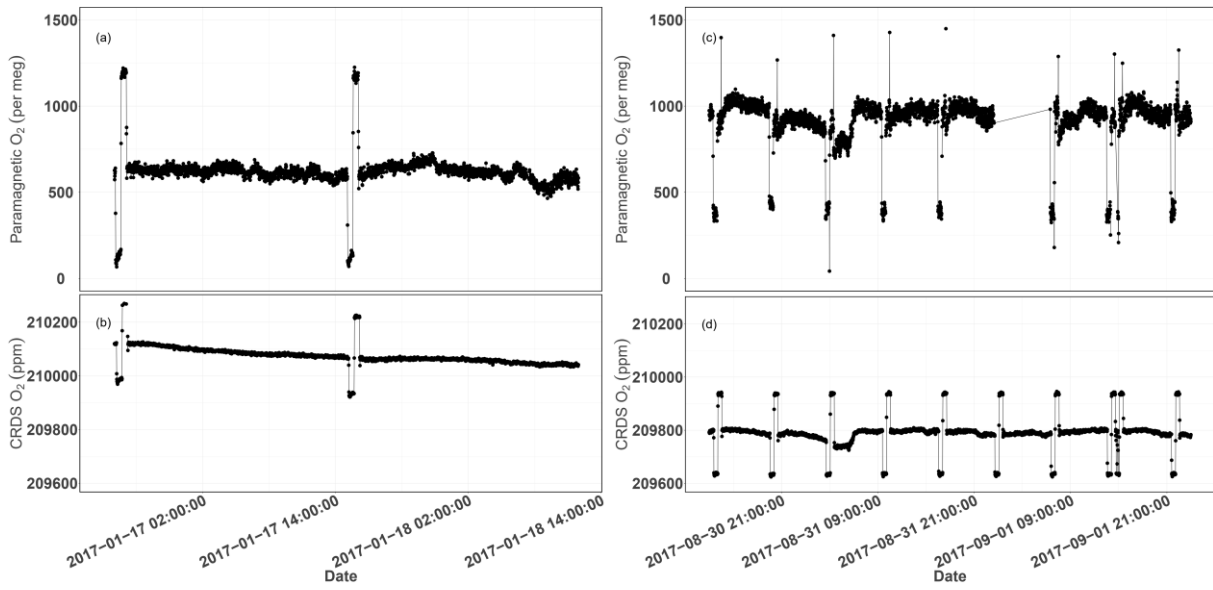
Figure 13. Parallel ambient air measurements by the Paramagnetic and CRDS analyzers at the

beginning of the testing period (Panels a & b, January 2017) and the second phase of testing

(Panels c & d, September 2017). The spikes are measurements from the two standard gases

bracketing the ambient air values.

842

843

844

845

846

847

848

849

850

851

852

853
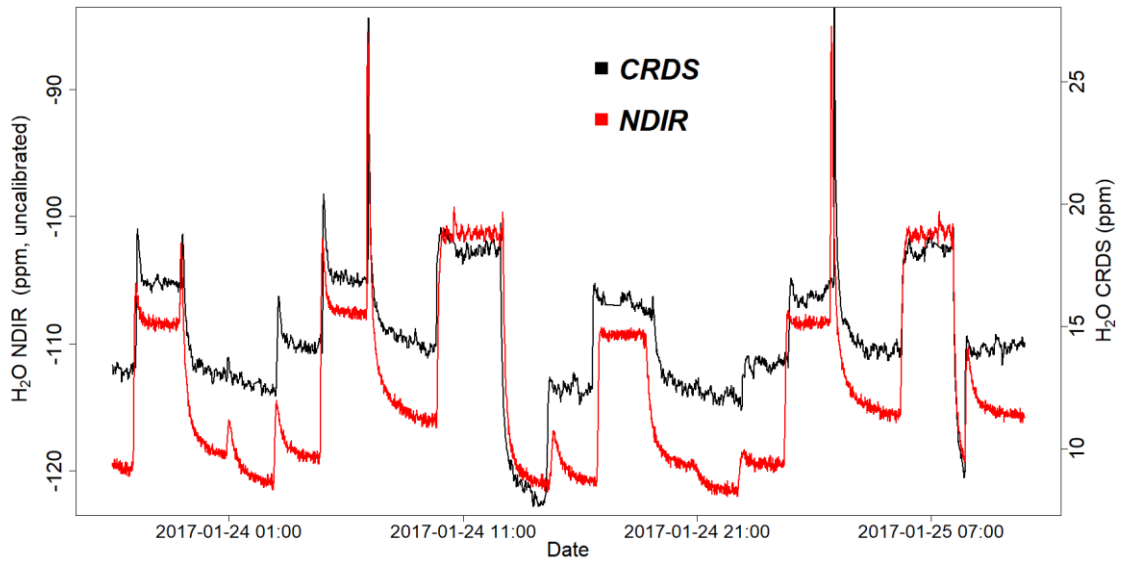
854

855   Figure 14. Parallel water vapor measurements for a dried ambient air by both the NDIR and

856   CRDS analyzers. Note that the water values from the NDIR analyzer are not calibrated.

857

858

859

860

861

862

863

864

865

866

867

868

869

870

871
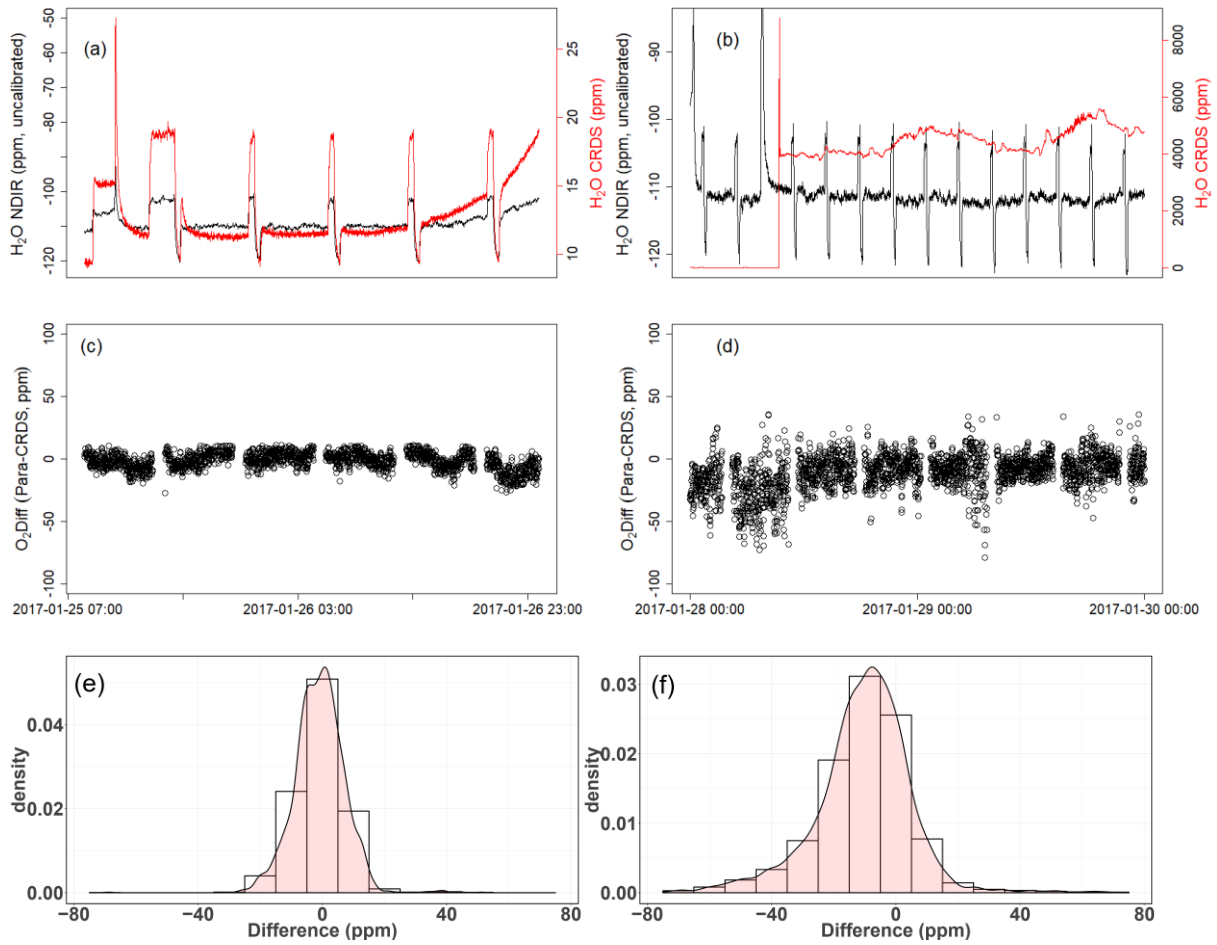
Figure 15. Results of water correction tests. Water measurements of the NDIR (left scale) for

dry conditions (a,b) and the CRDS analyzer (right scale) for dry (a) and wet (b) conditions.

The difference in oxygen measurements between the Paramagnetic and the CRDS instrument

using the built-in water correction for the CRDS values under dry (c) and wet (d) conditions.

Panels (e) and (f) show the population density functions.

877

878

879

880

881
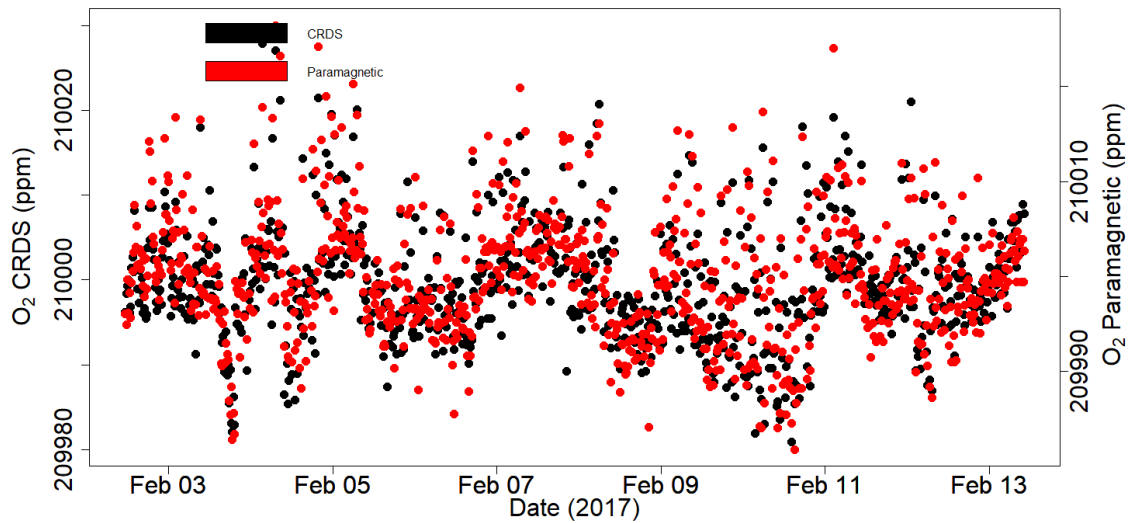
882
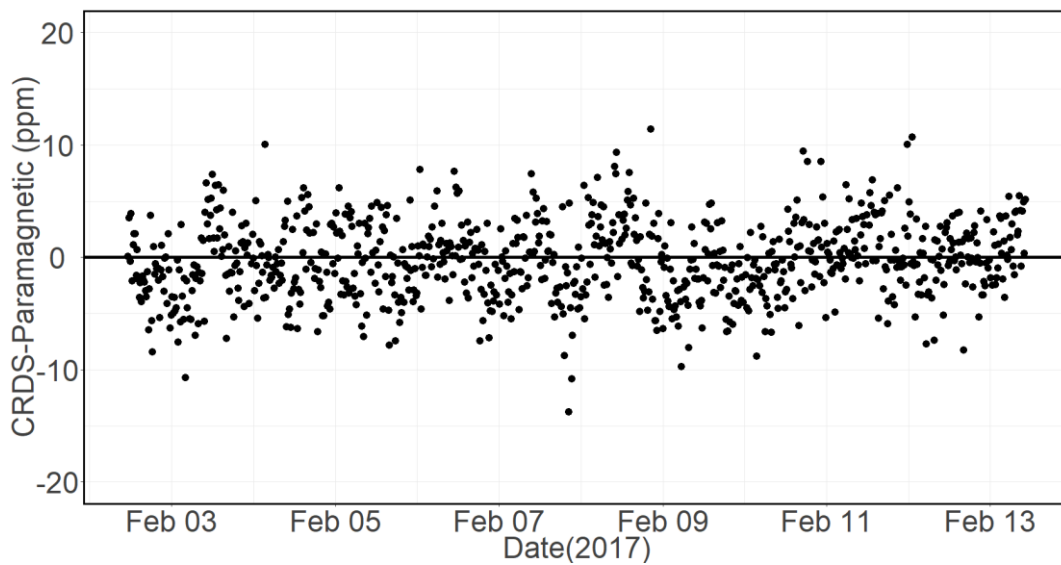
883

884 Figure 16. Calibrated ambient air oxygen measurements (1-minute average) at the

885 Jungfraujoch site using the CRDS and Paramagnetic analyzers both in ppm units (a) and the

886 absolute difference between the two measurements in ppm (b) by matching time stamps

887

888

889

890

891
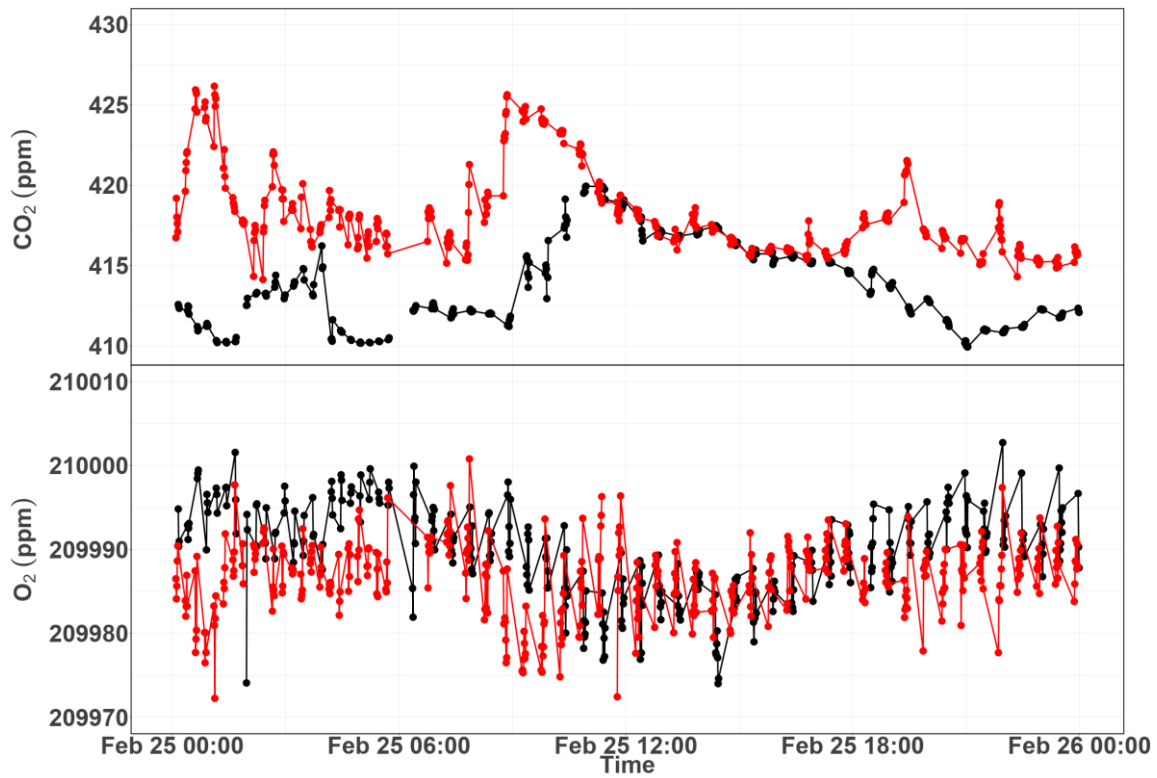
892

893   Figure 17. Diurnal variations of CO_2 (top) and O_2 (bottom) measurements from the 12 m (red)

894   and the 212.5 m (black) height levels at Beromünster tower.

895

896

897

898

899

900

901

902

903

904
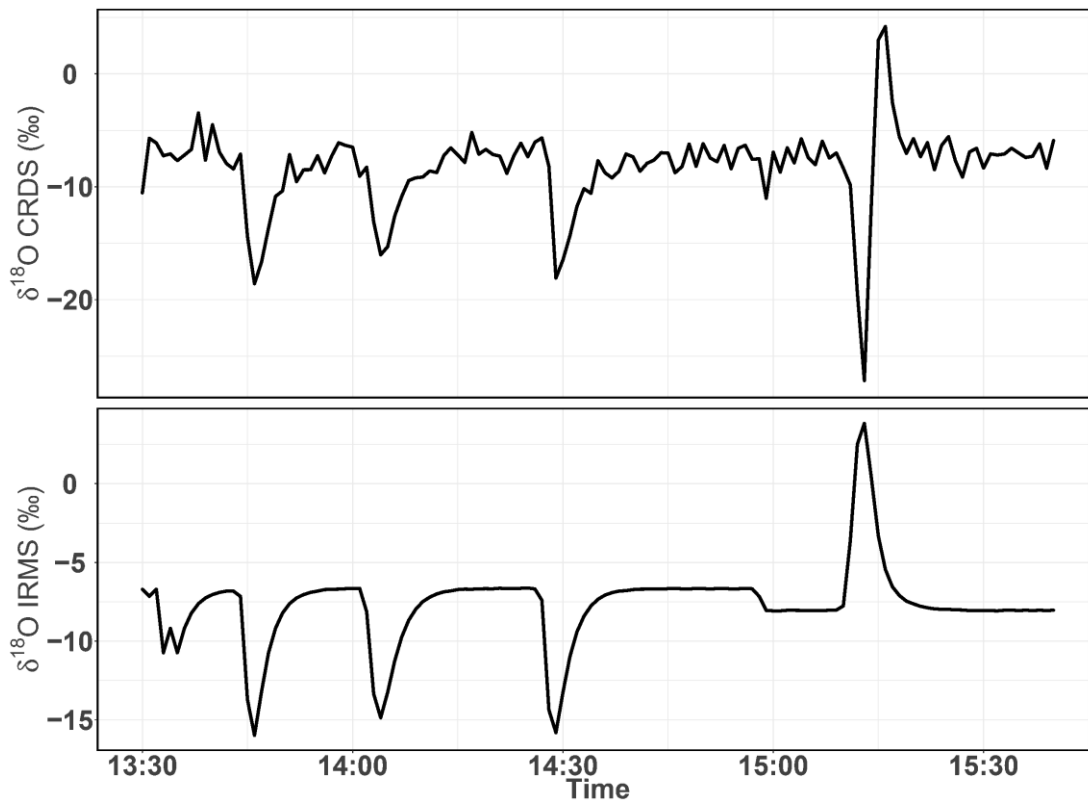
Figure 18. Consecutive $\delta^{18}O$ measurements of a standard gas (CO_2-free air) filled into three flasks followed by measurement of breath air using the CRDS analyzer (top) and IRMS (bottom). These measurements were carried out in the middle of ambient air measurements.

Appendix A.

920

921
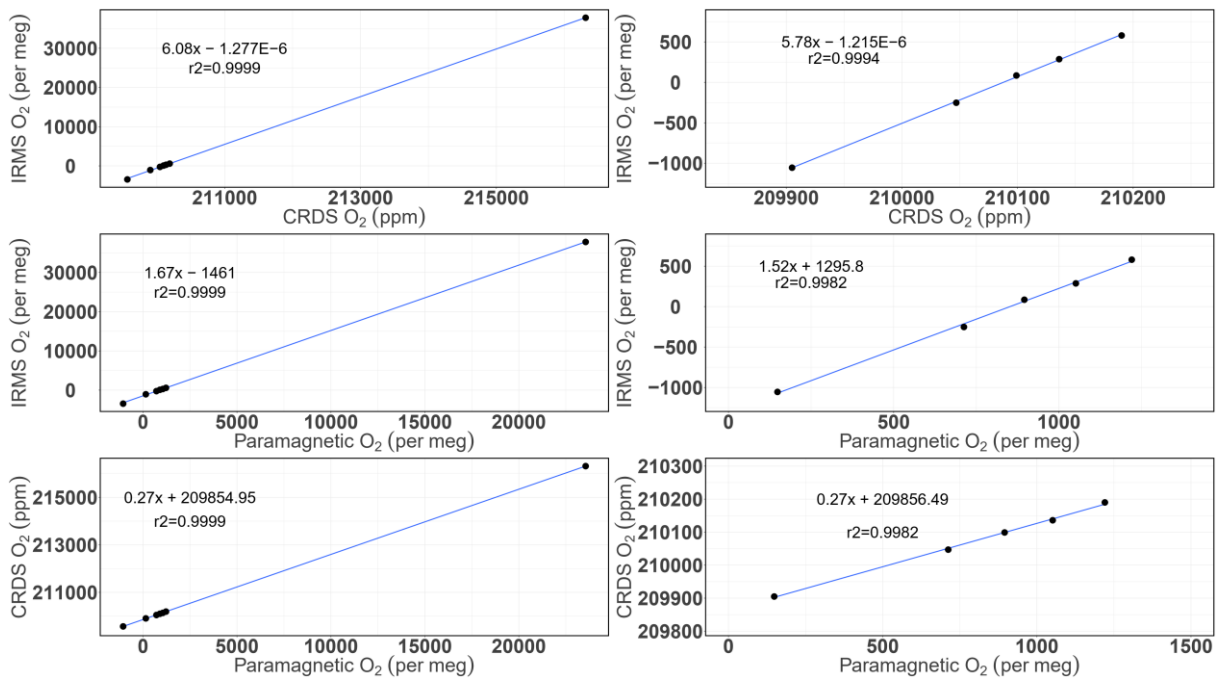
Figure A.1. Correlations between the O_2 mixing ratios measured by the CRDS and Paramagnetic analyzers with the mass spectrometric measurements (uncalibrated values). The left panels are for all the cylinders measured (standards 1 to 8) while the right ones are after selecting standards 1-5.

926

927

928

929

930

931

932

933

References

934   **References**

935   Battle, M., Bender, M. L., Tans, P. P., White, J. W. C., Ellis, J. T., Conway, T., and Francey, R. J.: Global

936   carbon sinks and their variability inferred from atmospheric O-2 and delta C-13, Science, 287, 2467-

937   2470, 2000.

938   Bender, M. L., Tans, P. P., Ellis, J. T., Orchardo, J., and Habfast, K.: A High-Precision Isotope Ratio

939   Mass-Spectrometry Method for Measuring the O-2 N-2 Ratio of Air, Geochim Cosmochim Ac, 58,

940   4751-4758, 1994.

941   Berhanu, T. A., Satar, E., Schanda, R., Nyfeler, P., Moret, H., Brunner, D., Oney, B., and Leuenberger,

942   M.: Measurements of greenhouse gases at Beromünster tall tower station in Switzerland, Atmos.

943   Meas. Tech. , 9, 2016.

944   Berhanu, T. A., Szidat, S., Brunner, D., Satar, E., Schanda, R., Nyfeler, P., Battaglia, M., Steinbacher,

945   M., Hammer, S., and Leuenberger, M.: Estimation of the fossil-fuel component in atmospheric CO2

946   based on radiocarbon measurements at the Beromünster tall tower, Switzerland, Atmos. Chem.

947   Phys. Discuss., 2017, 1-33, 2017.

948   Crosson, E. R. J. A. P. B.: A cavity ring-down analyzer for measuring atmospheric levels of methane,

949   carbon dioxide, and water vapor, 92, 403-408, 2008.

950   Filges, A., Gerbig, C., Rella, C. W., Hoffnagle, J., Smit, H., Krämer, M., Spelten, N., Rolf, C., Bozóki, Z.,

951   Buchholz, B., and Ebert, V.: Evaluation of the IAGOS-Core GHG Package H2O measurements during

952   the DENCHAR airborne inter-comparison campaign in 2011, Atmos. Meas. Tech., 11, 5279–5297,

953   2018, https://doi.org/10.5194/amt-11-5279-2018. Gao, F., Zhang, X., Zhang, X., Wang, M., and Wang,

954   P.: Virtual electronic nose with diagnosis model for the detection of hydrogen and methane in breath

955   from gastrointestinal bacteria, 28-31 May 2017 2017, 1-3.

956   Gordon, E., Rothman, S., Hill, C., Kochanov, V., Tan, Y., Bernath, P., Birk, M., Boudon, V., Campargue,

957   A., Chance, K., Drouin, J., Flaud, J., Gamache, R. R., Hodges, J., Jacquemart, D., Perevalov, I., Perrin, A.,

958   Shine, P., Smith, M., Tennyson, J., Toon, G., Tran, H., Tyuterev, G., Barbe, A., Császár, G., Devi, M.,

959 Furtenbacher, T., Harrison, J., Hartmann, J., Jolly, A., Johnson, J., Karman, T., Kleiner, I., Kyuberis, A.

960 A., Loos, J., Lyulin, M., Massie, S., Mikhailenko, S., Moazzen-Ahmadi, N., Muller, S., Naumenko, O. V.,

961 Nikitin, A. V., Polyansky, O. L., Rey, M., Rotger, M., Sharpe, S., Sung, K., Starikova, E., Tashkun, S.,

962 Auwera, J., Wagner, G., Wilzewski, J., Wcisło, P., Yu, S., and Zak, E. J.: The HITRAN2016 molecular

963 spectroscopic database, 203, 3 - 69, 2017.

964 Goto, D., Morimoto, S., Ishidoya, S., Aoki, S., and Nakazawa, T.: Terrestrial biospheric and oceanic

965 CO_2 uptake estimated from long-term measurements of atmospheric CO_2 mole fraction, $\delta13C$ and

966 $\delta(O_2/N_2)$ at Ny-Ålesund, Svalbard, Journal of Geophysical Research: Biogeosciences, doi:

967 10.1002/2017JG003845, 2017. n/a-n/a, 2017.

968 Gottlieb, K., Le, C. X., Wacher, V., Sliman, J., Cruz, C., Porter, T., and Carter, S.: Selection of a cut-off

969 for high- and low-methane producers using a spot-methane breath test: results from a large north

970 American dataset of hydrogen, methane and carbon dioxide measurements in breath, Gastroenterol

971 Rep, 5, 193-199, 2017.

972 Hartmann, J.-M., Boulet, C., and Robert, D.: Collisional Effects on Molecular Spectra, Elsevier Science,

973 2008.

974 Henne, S., Brunner, D., Folini, D., Solberg, S., Klausen, J., and Buchmann, B.: Assessment of

975 parameters describing representativeness of air quality in-situ measurement sites, Atmos. Chem.

976 Phys., 10, 3561-3581, 2010.

977 Hodges, J. T., Layer, H. P., Miller, W. W., and Scace, G. E.: Frequency-stabilized single-mode cavity

978 ring-down apparatus for high-resolution absorption spectroscopy, 75, 849-863, 2004.

979 Keeling, R. F.: Development of an Interferometric Oxygen Analyzer for Precise Measurement of the

980 Atmospheric O_2 Mole Fraction, UMI, 1988a.

981 Keeling, R. F.: Measuring correlations between atmospheric oxygen and carbon dioxide mole

982 fractions: A preliminary study in urban air, J Atmos Chem, 7, 153-176, 1988b.

983   Keeling, R. F. and Manning, A. C.: 5.15 - Studies of Recent Changes in Atmospheric O2 Content A2 -

984   Holland, Heinrich D. In: Treatise on Geochemistry (Second Edition), Turekian, K. K. (Ed.), Elsevier,

985   Oxford, 2014.

986   Keeling, R. F. and Shertz, S. R.: Seasonal and Interannual Variations in Atmospheric Oxygen and

987   Implications for the Global Carbon-Cycle, Nature, 358, 723-727, 1992.

988   Keeling, R. F., Stephens, B. B., Najjar, R. G., Doney, S. C., Archer, D., and Heimann, M.: Seasonal

989   variations in the atmospheric O-2/N-2 ratio in relation to the kinetics of air-sea gas exchange, Global

990   Biogeochem Cy, 12, 141-163, 1998.

991   Lamouroux, J., Sironneau, V., Hodges, J. T., and Hartmann, J. M.: Isolated line shapes of molecular

992   oxygen: Requantized classical molecular dynamics calculations versus measurements, Physical

993   Review A, 89, 042504, 2014.

994   Le Quéré, C., Andrew, R. M., Friedlingstein, P., Sitch, S., Pongratz, J., Manning, A. C., Korsbakken, J. I.,

995   Peters, G. P., Canadell, J. G., Jackson, R. B., Boden, T. A., Tans, P. P., Andrews, O. D., Arora, V. K.,

996   Bakker, D. C. E., Barbero, L., Becker, M., Betts, R. A., Bopp, L., Chevallier, F., Chini, L. P., Ciais, P.,

997   Cosca, C. E., Cross, J., Currie, K., Gasser, T., Harris, I., Hauck, J., Haverd, V., Houghton, R. A., Hunt, C.

998   W., Hurtt, G., Ilyina, T., Jain, A. K., Kato, E., Kautz, M., Keeling, R. F., Klein Goldewijk, K., Körtzinger, A.,

999   Landschützer, P., Lefèvre, N., Lenton, A., Lienert, S., Lima, I., Lombardozzi, D., Metzl, N., Millero, F.,

1000   Monteiro, P. M. S., Munro, D. R., Nabel, J. E. M. S., Nakaoka, S. I., Nojiri, Y., Padín, X. A., Peregon, A.,

1001   Pfeil, B., Pierrot, D., Poulter, B., Rehder, G., Reimer, J., Rödenbeck, C., Schwinger, J., Séférian, R.,

1002   Skjelvan, I., Stocker, B. D., Tian, H., Tilbrook, B., van der Laan-Luijkx, I. T., van der Werf, G. R., van

1003   Heuven, S., Viovy, N., Vuichard, N., Walker, A. P., Watson, A. J., Wiltshire, A. J., Zaehle, S., and Zhu,

1004   D.: Global Carbon Budget 2017, Earth Syst. Sci. Data Discuss., 2017, 1-79, 2017.

1005   Manning, A.: Temporal variability of atmospheric oxygen from both continuos and measurements

1006   and a flask sampling network: tools for studying the global carbon cycle, Ph.D. Ph.D., University of

1007   California, San Diego, San Diego, Calofornia, USA, 2001.

1008   Manning, A. C. and Keeling, R. F.: Global oceanic and land biotic carbon sinks from the Scripps

1009   atmospheric oxygen flask sampling network, Tellus B, 58, 95-116, 2006.

1010   Manning, A. C., Keeling, R. F., and Severinghaus, J. P.: Precise atmospheric oxygen measurements

1011   with a paramagnetic oxygen analyzer, Global Biogeochem Cy, 13, 1107-1115, 1999.

1012   Marrero, T. R. and Mason, E. A.: Gaseous Diffusion Coefficients, Journal of Physical and Chemical

1013   Reference Data 1, 3, 1972.

1014   Martin, N. A., Ferracci, V., Cassidy, N., and Hoffnagle, J. A. J. A. P. B.: The application of a cavity ring-

1015   down spectrometer to measurements of ambient ammonia using traceable primary standard gas

1016   mixtures, 122, 219, 2016.

1017   Mckay, L. F., Eastwood, M. A., and Brydon, W. G.: Methane Excretion in Man - a Study of Breath,

1018   Flatus, and Feces, Gut, 26, 69-74, 1985.

1019   Nevison, C. D., Keeling, R. F., Kahru, M., Manizza, M., Mitchell, B. G., and Cassar, N.: Estimating net

1020   community production in the Southern Ocean based on atmospheric potential oxygen and satellite

1021   ocean color data, Global Biogeochem Cy, 26, 2012.

1022   Oney, B., Henne, S., Gruber, N., Leuenberger, M., Bamberger, I., Eugster, W., and Brunner, D.: The

1023   CarboCount CH sites: characterization of a dense greenhouse gas observation network, Atmos.

1024   Chem. Phys., 15, 11147-11164, 2015.

1025   Press, W. H., Teukolsky, S. A., Vetterling, W. T., and Flannery, B. P.: Numerical Recipes 3rd Edition:

1026   The Art of Scientific Computing, Cambridge Printing Press, Cambridge, England, 1986.

1027   Press, W. H., Teukolsky, S. A., Vetterling, W. T., and Flannery, B. P.: Numerical recipes in C: the art of

1028   scientific computing, Cambridge University Press, London, 1992.

1029   Ryter, S. W. and Choi, A. M. K.: Carbon monoxide in exhaled breath testing and therapeutics, J Breath

1030   Res, 7, 2013.

1031   Satar, E., Berhanu, T. A., Brunner, D., Henne, S., and Leuenberger, M.: Continuous CO2/CH4/CO

1032   measurements (2012–2014) at Beromünster tall tower station in Switzerland, Biogeosciences, 13,

1033   2623-2635, 2016.

1034   Schibig, M. F., Steinbacher, M., Buchmann, B., van der Laan-Luijkx, I. T., van der Laan, S., Ranjan, S.

1035   and Leuenberger, M. C,: Comparison of continuous in situ CO2 observations at Jungfraujoch using

1036   two different measurement techniques, Atmospheric Measurement Techniques

1037   , 8, 57-68, 10.5194/amt-8-57-2015, 2015.

1038   Severinghaus, J. P.: Studies of the terresterial O2 and carbon cycles in sand dune gases and in

1039   Biosphere Doctoral Ph.D., Columbia University, New York, USA, 1995.

1040   Steig, E. J., Gkinis, V., Schauer, A. J., Schoenemann, S. W., Samek, K., Hoffnagle, J., Dennis, K. J., and

1041   Tan, S. M.: Calibrated high-precision ^{17}O-excess measurements using cavity ring-down

1042   spectroscopy with laser-current-tuned cavity resonance, Atmos. Meas. Tech., 7, 2014.

1043   Stephens, B. B., Bakwin, P. S., Tans, P. P., Teclaw, R. M., and Baumann, D. D.: Application of a

1044   differential fuel-cell analyzer for measuring atmospheric oxygen variations, J Atmos Ocean Tech, 24,

1045   82-94, 2007.

1046   Sturm, P., M. Leuenberger, F.L. Valentino, B. Lehmann, and B. Ihly, Measurements of CO_2, its stable

1047   isotopes, O_2/N_2, and ^{222}Rn at Bern, Switzerland, *Atmospheric Chemistry and Physics*, *6*, 1991-2004,

1048   2006.

1049   Tennyson, J., Bernath, P. F., Campargue, A., Császár, A. G., Daumont, L., Gamache, R. R., Hodges, J. T.,

1050   Lisak, D., Naumenko, O. V., Rothman, L. S., Tran, H., Zobov, N. F., Buldyreva, J., Boone, C. D., De Vizia,

1051   M. D., Gianfrani, L., Hartmann, J.-M., McPheat, R., Weidmann, D., Murray, J., Ngo, N. H., and

1052   Polyansky, O. L.: Recommended isolated-line profile for representing high-resolution spectroscopic

1053   transitions (IUPAC Technical Report), 86, 1931–1943, 2014.

1054 Tohjima, Y.: Method for measuring changes in the atmospheric O-2/N-2 ratio by a gas

1055 chromatograph equipped with a thermal conductivity detector, J Geophys Res-Atmos, 105, 14575-

1056 14584, 2000.

1057 Tran, H., Turbet, M., Hanoufa, S., Landsheere, X., Chelin, P., Ma, Q., Hartmann, J.: The CO_2–

1058 broadened H_2O continuum in the 100–1500 cm-1 region: Measurements, predictions and empirical

1059 model, Journal of Quantitative Spectroscopy and Radiative Transfer, 230, 75-80, 2019.

1060 Valentino, F. L., Leuenberger, M., Uglietti, C., and Sturm, P.: Measurements and trend analysis of O_2,

1061 CO_2 and $\delta 13C$ of CO_2 from the high altitude research station Junfgraujoch, Switzerland — A

1062 comparison with the observations from the remote site Puy de Dôme, France, Sci Total Environ, 391,

1063 203-210, 2008.

1064 Varghese, P. L. and Hanson, R. K.: Collisional narrowing effects on spectral line shapes measured at

1065 high resolution, Appl. Opt., 23, 2376-2385, 1984.

1066 Wójtewicz, S., Cygan, A., Masłowski, P., Domysławska, J., Wcisło, P., Zaborowski, M., Lisak, D.,

1067 Trawiński, R. S., and Ciuryło, R.: Spectral line-shapes of oxygen B-band transitions measured with

1068 cavity ring-down spectroscopy, Journal of Physics: Conference Series, 548, 012028, 2014.

1069 Wolf, P. G., Parthasarathy, G., Chen, J., O'Connor, H. M., Chia, N., Bharucha, A. E., and Gaskins, H. R.:

1070 Assessing the colonic microbiome, hydrogenogenic and hydrogenotrophic genes, transit and breath

1071 methane in constipation, Neurogastroent Motil, 29, 2017.

1072 Zellweger, C., Forrer, J., Hofer, P., Nyeki, S., Schwarzenbach, B., Weingartner, E., Ammann, M., and

1073 Baltensperger, U.: Partitioning of reactive nitrogen (NO_y) and dependence on

1074 meteorological conditions in the lower free troposphere, Atmos. Chem. Phys., 3, 779-796, 2003.

1075